








Implicit Large-eddy Simulations of Global Solar Convection: Effects of Numerical Resolution in Nonrotating and Rotating Cases

G. Guerrero^{1,2} , A. M. Stejko² , A. G. Kosovichev² , P. K. Smolarkiewicz³ , and A. Strugarek⁴ 

¹ Physics Department, Universidade Federal de Minas Gerais Av. Antonio Carlos, 6627, Belo Horizonte, MG 31270-901, Brazil; guerrero@fisica.ufmg.br

² New Jersey Institute of Technology, Newark, NJ 07103, USA

³ National Center for Atmospheric Research, Boulder, Colorado, USA

⁴ AIM, CEA, CNRS, Université Paris-Saclay, Université Paris Diderot, Sorbonne Paris Cité, France

Received 2022 August 10; revised 2022 October 6; accepted 2022 October 14; published 2022 November 30

Abstract

Simulating deep solar convection and its coupled mean-field motions is a formidable challenge where few observational results constrain models that suffer from the nonphysical influence of the grid resolution. We present hydrodynamic global implicit large-eddy simulations of deep solar convection performed with the EULAG-MHD code, and we explore the effects of grid resolution on the properties of rotating and nonrotating convection. The results, based on low-order moments and turbulent spectra, reveal that convergence in nonrotating simulations may be achieved at resolutions not much higher than these considered here. The flow is highly anisotropic, with the energy contained in horizontal divergent motions exceeding their radial counterpart by more than three orders of magnitude. By contrast, in rotating simulations, the largest energy is in the toroidal part of the horizontal motions. As the grid resolution increases, the turbulent correlations change in such a way that a solar-like differential rotation, obtained in the simulation with the coarser grid, transitions to an antisolar differential rotation. The reason for this change is the contribution of the effective viscosity to the balance of the forces driving large-scale flows. As the effective viscosity decreases, the angular momentum balance improves, yet the force balance in the meridional direction lessens, favoring a strong meridional flow that advects angular momentum toward the poles. The results suggest that obtaining the correct distribution of angular momentum may not be a mere issue of numerical resolution. Accounting for additional physics, such as magnetism or the near-surface shear layer, may be necessary in simulating the solar interior.

Unified Astronomy Thesaurus concepts: [Solar differential rotation \(1996\)](#); [Solar meridional circulation \(1874\)](#); [Solar interior \(1500\)](#); [Hydrodynamical simulations \(767\)](#)

1. Introduction

Turbulent convection is observed at the solar photosphere in the form of granulation, with scales of several thousands of kilometers, and supergranulation, with scales of $\sim 30,000$ km. From theoretical considerations, it is expected that larger, self-similar, motions exist at deeper layers. Their characteristics, however, remain elusive to observations. The properties of solar convection in deeper layers are relevant for understanding the physical processes that drive and shape the large-scale flows observed in the Sun, namely the differential rotation (DR) and the meridional circulation (MC). Furthermore, they may be instrumental for the solar dynamo process.

The knowledge that we have about the deep turbulent motions is based on the one-dimensional mixing-length theory (MLT; Böhm-Vitense 1958; Kippenhahn et al. 2013). The results of MLT models predict that the spatial and temporal scales of convection progressively increase with depth. Nevertheless, helioseismic observations of turbulent motions just in the upper convection zone have offered conflicting results, such that the MLT scenario cannot be confirmed. On one hand, using time–distance helioseismology measurements, Hanasoge et al. (2012) found that the convective power of the large scales is several orders of magnitude smaller than the MLT prediction. On the other hand, the results obtained by ring-diagram analysis (Greer et al. 2015) suggested spectral

energies more in line with the theory, perhaps even with a power greater than expected. This ambiguity is often called the solar convective conundrum.

Proxauf (2020) and collaborators have recently identified several incompatibilities in the comparison of the previous results, proposed the required corrections, and obtained new inferences. Despite modifications, the disparity between the two helioseismic inferences still spans three to four orders of magnitude. Their analysis using surface granulation tracking and ring-diagram measurements indicated that at low angular harmonic degree, ℓ , the trend of the power spectra agrees with the corrected results of Hanasoge et al. (2012), with slightly higher power (about one order of magnitude). Other analyses seem to confirm the existence of convective structures larger than supergranulation but with relatively small power (Getling & Kosovichev 2022, ; Hathaway & Upton 2021). In the deeper layers, the properties of convection are still a mystery, and we rely on global simulations of turbulent rotating convection to get access at least to some of its characteristics. Unfortunately, such simulations are not exempt from difficulties.

The overall goal of global convection simulations, precluding so far the possible development of magnetic fields, is developing motions able to carry out most of the solar luminosity, L_{\odot} , and at the same time producing a mean angular velocity in agreement with the helioseismic observations (Schou et al. 1998), and a meridional circulation with poleward migration on the surface (e.g., Hathaway & Upton 2014; Ulrich 2010). The meridional circulation profile in the deep convection zone is still under investigation and remains a matter of debate (see Chen & Zhao 2017; Gizon et al. 2020; Stejko et al. 2021, for inferences with two and one meridional cells per hemisphere).



Original content from this work may be used under the terms of the [Creative Commons Attribution 4.0 licence](#). Any further distribution of this work must maintain attribution to the author(s) and the title of the work, journal citation and DOI.

The parameter regime of the solar interior where convection must transport energy and angular momentum is characterized by the Rayleigh (Ra) number $\mathcal{O}(10^{20})$, the Reynolds number (Re) $\mathcal{O}(10^{12})$, and the Prandtl (Pr) number $\mathcal{O}(10^{-7})$ (see Table 2 in Ossendrijver 2003). The separation of the dynamical scales determined by these parameters requires enormous computational resources to be resolved by direct numerical simulations (DNS). Modern supercomputers are still far from allowing DNS at such resolution. Thus, for the current DNS, the dissipative coefficients that define the nondimensional numbers are orders of magnitude larger than the microscopic values of viscosity and/or thermal conductivity. Considering that the values of these coefficients are consistent with the estimated turbulent dissipation, these simulations can be viewed as large-eddy simulations (LES) that preclude nondissipative contribution of the unresolved scales.

In state-of-the-art simulations in which the radiative flux driving convection at the bottom of the convection zone corresponds to $L_{\odot} = 3.83 \times 10^{26}$ W, and the imposed rotation is the solar sidereal angular velocity, $\Omega_{\odot} = 2.97 \times 10^6 \text{ s}^{-1}$, the convective heat flux results in enhanced turbulent velocities whose energy spectrum disagrees with the helioseismic observations described above (Gizon & Birch 2012). Additionally, higher velocities imply shorter convective correlation times, τ_c , and therefore larger Rossby numbers, which represent the ratio between rotation and convection timescales, $\text{Ro} = P_{\text{rot}}/\tau_c$. This ratio is an indication of how strongly the convective motions are constrained by the Coriolis force. It is a fairly robust result of global convective simulations (Käpylä et al. 2011; Featherstone & Miesch 2015; Gastine et al. 2014; Guerrero et al. 2013) that, as the motions become less rotationally constrained (high Ro), the differential rotation profile has faster poles and a slower equator, at odds with the observed solar profile.

A solar-like differential rotation profile with an accelerated equator may be recovered by increasing the rotation rate by a factor of two or three (Brown et al. 2008; Hotta 2018). Another alternative is diminishing the convective transport by increasing the radiative diffusion coefficient (Featherstone & Miesch 2015; Käpylä et al. 2014; Miesch et al. 2008) or by decreasing the luminosity of the simulation (Guerrero et al. 2013; Hotta et al. 2015). The latter options artificially decrease the strength of the convective flows. In general, these alternatives reduce the Rossby number.

Large- or small-scale magnetic fields may also help to reproduce the solar differential rotation. They contribute in two different ways: by modulating the convective heat transport (Fan & Fang 2014; Guerrero et al. 2019; Karak et al. 2015), which decreases the turbulent velocities (lower Ro), and through the direct transport of angular momentum via the large- and small-scale Maxwell stresses. The contribution of the large-scale magnetic field has been verified by MHD simulations with relatively low resolution, which allowed the simulation to be performed for a long temporal evolution, including the excitation and sustainment of the large-scale dynamo. On the other hand, the contribution of the small-scale dynamo has been recently identified in the high-resolution simulations by Hotta & Kusano (2021) and Hotta et al. (2022). They suggested that the small-scale magnetic field diminishes the convective power and that a meridional flow, developed to balance the Maxwell stresses, transports angular momentum toward the equator. However, these simulations have been run only for a short time, so the large-scale magnetic field did not

develop. Thus, there is still no clarity on the distribution of small-scale magnetic fields in the presence of large-scale dynamo, and it is uncertain what is the role of both contributions on the angular momentum transport.

Most simulations described above suffer from the contribution of unrealistically large dissipative coefficients caused by the limited spatial resolution. Strong viscous dissipation, for instance, is needed to guarantee numerical stability. It is combined with the numerical dissipation associated with the numerical schemes. Both contributions directly affect the transport of linear and angular momentum, whereas in the Sun, the microscopic viscosity is negligible. Therefore, achieving converged solutions independently of numerical resolution is desirable albeit challenging. In other words, it is appealing to have a system where the dissipation coefficients are insignificant and the dynamics is governed by well-resolved turbulent motions subject to well-defined boundary conditions. However, as discussed above, this does not seem to be the case for the current models of deep solar convection. As a matter of fact, very few works have systematically explored the role of resolution on the properties of convection. The work of Featherstone & Hindman (2016a) is one exception, for nonrotating convection in the sphere, with remarkable results. They were able to achieve simulations where the amplitude of the kinetic energy became independent of the Ra values, yet the distribution of root mean square (rms) velocities and turbulent kinetic spectra continued changing as Ra further increased. Subsequently, Hindman et al. (2020) presented a large set of simulations with different rotation rates and Rayleigh numbers. They described the morphological changes of convection for different regimes of rotation and convection supercriticality. Unlike the nonrotating models, the kinetic energy of their rotating simulations kept increasing with Ra. Consequently, the kinetic energy spectra obtained from these simulations did not achieve a convergent profile.

Large-eddy simulations including explicit or implicit (Grinstein et al. 2007) turbulent subgrid-scale (SGS) contribution may be a computationally less expensive alternative to DNS of solar (stellar) convection and dynamo. LES have been routinely and successfully used in engineering and meteorological problems. This approach has also been used for modeling local convection and small-scale dynamos (Kitiashvili et al. 2015; Rogachevskii et al. 2011; Wray et al. 2015). Nevertheless, it has not been broadly considered in the problem of global simulations of solar and stellar convection and dynamos. This is understandable given that, unlike laboratory experiments or weather and climate studies, there are neither sufficient available data nor convergent DNS results of the same problem. This prevents the comparison and characterization of the LES results and the SGS models.

The implicit LES simulations performed with the EULAG-MHD code, based on a nonoscillatory forward-in-time algorithm, have been successful in reproducing at lower resolution some characteristics of the solar activity cycle (Ghizaru et al. 2010), and they have also been used to study stellar activity (Guerrero et al. 2019; Strugarek et al. 2017). In the code, the dynamical equations may be solved in their inviscid form, with the viscous contribution given by the minimized truncation terms, allowing the highest possible level of turbulence, i.e., the largest value of Re, to be achieved for any resolution. In this form, it is less computationally expensive to search for solutions to the problem that are independent of the nonphysical influence of numerical

resolution. We have demonstrated the numerical convergence in 2D convection simulations for a range of mesh sizes (Nogueira et al. 2022). The low-order moments in the physical space as well as the turbulent spectra of kinetic and thermal energy were used as criteria of convergence. We attribute the convergence of the results in the low-resolution cases to the implicit SGS viscosity of the nonoscillatory discrete advection method, which allows the backscatter of energy from small to large scales and dissipation at the minimal scale, close to the limit of numerical resolution. For progressively larger resolutions, however, large- and small-scale motions coexist in a system dominated by a mesh-independent turbulent dissipation. In these cases, the contribution from the small scales seems to be resolved.

In this paper, we continue the study presented in Nogueira et al. (2022) while approximating our numerical model to the solar interior by considering spherical geometry. Additionally, we consider the effects of rotation on the turbulent motions and explore the development of mean flows in models where all parameters are kept constant except the grid resolution. This problem is more complicated than the Cartesian case. On the one hand, the spherical geometry imposes curvature effects and numerical stiffness in polar regions. On the other hand, gravity and rotation result in strongly anisotropic convective motions upon which the amount of viscous resistance, wherever is its origin, turns out to be highly relevant. We anticipate that, for nonrotating cases, hints of convergence are achieved at a resolution consistent with the Cartesian cases. For the rotating cases, the resulting large-scale motions are substantially dependent on the resolution, due to the decreasing contribution of effective viscosity to the net transport of angular momentum. We characterize these changes through a comparative analysis of the spectral properties of the fluid and the balance of the azimuthal and meridional forces that drive these large-scale motions. To differentiate the most robust features of global convection from those that seem to be model dependent, we extend our comparison to previous findings of similar models, as well as to solar observations when possible. Even though we do not achieve convergence in our simulations, their analysis contributes to understanding the sustainment of solar mean flows and allows us to hypothesize possible ways to solve to the convective conundrum.

This paper is organized as follows. In Section 2, we describe the numerical model. The results of nonrotating and rotating cases are presented in Section 3, and in Section 4, we discuss our findings and expound the conclusions of this work.

2. Numerical Model

The EULAG-MHD code (Smolarkiewicz & Charbonneau 2013)—a specialized variant of the original EULAG code (Prusa et al. 2008)—is used to perform global anelastic convection simulations. EULAG-MHD is based on the multidimensional positive-definite advection transport algorithm (MPDATA; Smolarkiewicz 2006). It is a nonoscillatory forward-in-time advection solver with second-order accuracy in space and time. The code allows simulations to be run as ILES without explicit dissipation, yet it also may be used for DNS with explicit dissipation. The domain corresponds to a global spherical shell with the radial coordinate, r , covering the upper fraction of the radiative zone from $r_b = 0.6R_\odot$, and the convection zone (CZ) up to $r_t = 0.96R_\odot$. We exclude the upper layers of the CZ where compressibility and radiative transfer play a significant role in the dynamics of convection.

The code integrates the following set of Navier–Stokes equations governing mass, momentum, and energy conservation:

$$\nabla \cdot \rho_r \mathbf{u} = 0, \quad (1)$$

$$\frac{d\mathbf{u}}{dt} + 2\boldsymbol{\Omega} \times \mathbf{u} = -\nabla\pi' - \mathbf{g} \frac{\Theta'}{\Theta_a}, \quad (2)$$

$$\frac{d\Theta'}{dt} = -\mathbf{u} \cdot \nabla\Theta_a - \alpha\Theta' \quad (3)$$

where $d/dt = \partial/\partial t + \mathbf{u} \cdot \nabla$; \mathbf{u} is the velocity field in a frame rotating with angular velocity $\boldsymbol{\Omega} = (\Omega_r, \Omega_\theta, \Omega_\phi) = \Omega_0(\cos\theta, -\sin\theta, 0)$; ρ_r is the reference state density, which in the anelastic approximation is a function of radius only (Lipps & Hemler 1982); π' is the density-normalized pressure perturbation; p'/ρ_r ; $\mathbf{g} = -g\hat{\mathbf{e}}_r$ is the gravity acceleration adjusted to fit the solar gravity profile; and Θ is the potential temperature, defined as $\Theta = T(P_b/P)^{R/c_p}$, where T is the temperature, P is the pressure, P_b is the pressure at the bottom of the domain, $R = 13732 \text{ J K}^{-1} \text{ kg}^{-1}$ is the universal gas constant for a monoatomic hydrogen gas, and $c_p = 2.5R$, is the specific heat at constant pressure. The potential temperature is equivalent to the specific entropy through the relation $ds = c_p d(\ln\Theta)$. The subscripts r and a refer to the reference and ambient states, and the superscript $'$ means perturbations of a quantity about the ambient profile. Perturbations of Θ are related to perturbations of temperature by the anelastic approximation, $T' = \Theta' T_a / \Theta_a$. The energy equation contains a term forcing the adiabatic perturbations about the ambient state and a thermal relaxation term that damps these perturbations in an inverse timescale, $\alpha = 1/\tau$ (see Cossette et al. 2017, for a discussion).

The ambient state defining the thermodynamic variables, ρ_a , Θ_a , and T_a in Equations (1)–(3) is a particular solution of the hydrodynamics equations. In this work, the ambient state considering hydrostatic equilibrium for a nonrotating atmosphere is constructed by solving the following equations:

$$\frac{\partial T_a}{\partial r} = -\frac{g}{R(m+1)}, \quad (4)$$

$$\frac{\partial \rho_a}{\partial r} = -\frac{\rho}{T_a} \left(\frac{g}{R} + \frac{\partial T_a}{\partial r} \right), \quad (5)$$

where $m = m(r)$ is the polytropic index. Solutions of Equations (4) and (5) with $m \geq 1.5$ correspond to stable stratification, while solutions for $m < 1.5$ correspond to convectively unstable states.

The ambient state with a stable layer at the bottom of the domain is built by setting $m_s = 2.5$ for $r \leq 0.7R_\odot$, and a marginally unstable convection zone with $m_u = 1.49997$ for $r > 0.7R_\odot$. This is achieved by considering a radial profile of the polytropic index,

$$m(r) = m_s - \frac{1}{2}(m_s - m_u) \left[1 + \operatorname{erf} \left(\frac{r - r_1}{w} \right) \right], \quad (6)$$

where the transition between zones of different m is made through the erf functions with $r_1 = 0.7R_\odot$ and $w = 0.01R_\odot$. Equations (4) and (5) are integrated numerically with $\rho_{r_1} = 208 \text{ kg/m}^3$ and $T_{r_1} = 2.322 \times 10^6 \text{ K}$ at the interface between the stable and the unstable layers. The pressure is computed via the ideal gas equation of state, $P_a = R\rho_a T_a$. The resulting profile of Θ_a as a

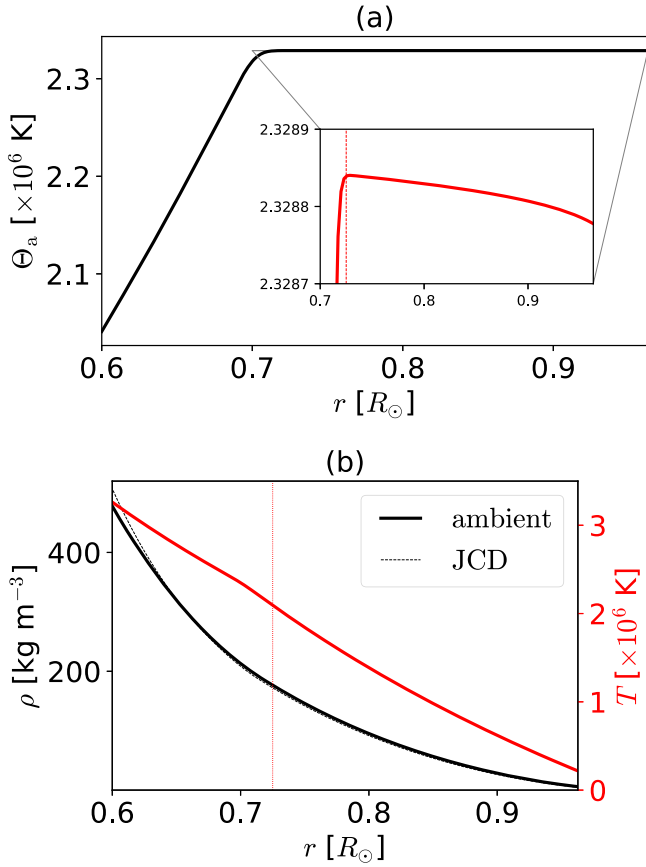


Figure 1. (a) Radial profile of the ambient potential temperature, Θ_a . The insert shows a close-up for $0.7 < r/R_\odot < 0.96$ depicting a negative radial gradient of Θ_a . The difference between the bottom and top of the unstable layer is 62 K. (b) Radial profiles of the ambient density (black line) and temperature (red line). The dotted lines correspond to the solar structure model of Christensen-Dalsgaard et al. (1996). From the bottom to the top of the domain, there are ~ 4.5 density scale heights. From the base of the convection zone, $r > 0.7R_\odot$, there are ~ 3.7 density scale heights. The vertical red lines show the bottom of the unstable layer located at $r = 0.725R_\odot$.

function of radius is shown in Figure 1(a). In the convective zone, the slope of Θ_a is slightly negative with respect to the r coordinate, as can be seen in the figure insert. The negative slope of Θ_a ensures that this zone is unstable to convection, with the difference of Θ_a between the bottom and top of the convectively unstable layer being 62 K. The reference potential temperature $\Theta_r = T_r$. Finally, for all the simulations, $\alpha = 1/\tau = 1.29 \times 10^{-8} \text{ s}^{-1}$ is considered. Figure 1(b) shows the radial profiles of the density, ρ_a , and the temperature, T_a . The entire radial domain encompasses 4.5 density scale heights, with 3.7 density scale heights corresponding to the unstable layer.

The boundary conditions for this setup are impermeable, stress-free conditions for the velocity field at the two radial ends of the domain. Null convective radial flux is considered to constitute thermal boundaries at the bottom and top, as it has been used in previous works in the literature (e.g., Fan et al. 2003; Hotta et al. 2015). For most of these cases, the initial conditions are white noise perturbations in Θ' , introduced only in the unstable layer and with maximum amplitude 0.1 K.

3. Results

In the simulations discussed below, the ambient stratification and the thermal relaxation timescale are kept constant;

therefore, the forcing and the thermal relaxation terms in Equation (3) are theoretically the same in all models (i.e., in the hypothetical limit of the converged numerical solutions). Nonrotating models ($\Omega_0 = 0$) with five different numerical resolutions (see Table 1) are presented. Based on the results of these models, three rotating simulations with $\Omega_0 = 3.03 \times 10^{-6} \text{ s}^{-1}$ ($P_{\text{rot}} = 24$ days) for three different resolutions are performed. For this rotation rate, the low-resolution case produces a solar-like differential rotation profile. The runtime of each simulations, here considered as the physical time, in years, for which the prognostic quantities evolve in time, is presented in Table 1. Simulation R8 is started from a remeshed snapshot of simulation R4 in the relaxed state and run for ~ 2.8 Earth years. The temporal averages are calculated from the outputs with a cadence of one month over a time range of five years. For simulation R8, only six months of simulated data were considered.

3.1. Nonrotating Convection

We first explore the effects of numerical resolution in the low-order moments and the spectral properties of nonrotating simulations. Figure 2 shows snapshots of the radial, latitudinal, and longitudinal velocities, w , v , and u , for simulations R1–R8 (from top to bottom). The graphs show the level of detail reached by different resolutions. The amplitude of the velocity components increases as evidenced by brighter colors from the top to the bottom panels. It is also evident that, in models R1 and R2, the grid size in regions with small density scale height, i.e., close to the model’s top, is insufficient to resolve the scales of the subsurface motions. This is observed in the rms profiles of the radial and longitudinal components of the velocity field, $w_{\text{rms}} = \sqrt{\langle w^2 \rangle_{\phi\theta}}$ and $u_{\text{rms}} = \sqrt{\langle u^2 \rangle_{\phi\theta}}$, as well as in the total rms velocity, $U_{\text{rms}} = \sqrt{\langle u^2 + v^2 + w^2 \rangle_{\phi\theta}}$, presented in Figure 3(a-c). Throughout this paper, angular brackets $\langle \rangle_{\phi\theta}$ correspond to averages over the horizontal directions and time, $\langle \rangle$ to volume and time averages over the convective shell, and overlines correspond to averages over longitude and time. In w_{rms} , the lack of resolution appears as a flat profile for $r > 0.9R_\odot$ in simulation R1 as well as for $r > 0.93R_\odot$ in simulation R2; see Figure 3(a). In u_{rms} and U_{rms} , it appears as a local minimum that may be observed in the profiles of the same simulations close to the upper boundary (Figures 3(b) and (c)). This undesirable property was reported in the 2D Cartesian cases (Nogueira et al. 2022). The black dashed line presented in the figure corresponds to simulation R1x. It has the same horizontal resolution as R1, but with a fourfold resolution in the radial direction ($N_\phi = 128$, $N_\theta = 64$, $N_r = 256$). While there are small departures from the cases with higher resolution, especially in the radial velocity, there is a remarkable similarity between case R1x and high-resolution cases R4 and R8.

The spherical simulations show radial motions that have a maximum roughly at the center of the convection zone ($r \sim 0.85R_\odot$). The amplitude of w_{rms} slightly increases from the low- to the high-resolution cases, with a rather small difference between cases R4 and R8. The longitudinal velocity, u_{rms} , shows larger amplitudes at the bottom of the convection zone resulting from the encounter of fast downward plumes with the rigid stable layer. As a consequence, the profiles of u_{rms} as a function of radius have a minimum in the bulk of the convection zone at about $0.8R_\odot$. This feature does not appear in simulations that consider only the convection zone, where a stress-free

Table 1
Simulation Parameters and Results

Simulation	N_ϕ, N_θ, N_r	dt [s]	Rt [yr]	$\langle U_{\text{rms}} \rangle$ (m s ⁻¹)	$\langle \Theta' \rangle$ [K]	$\langle L_c \rangle$ [L_\odot]	Ro	ν_t [$\times 10^9$]	ν_{eff} [$\times 10^8$]	κ_{eff} [$\times 10^8$]	Pr _{eff}	Re _{eff}
R1	128,64,64	1400	200	54.07	21.49	0.38	...	3.14	3.19	1.30	2.45	29
R2	256,128,128	500	80	51.70	13.78	0.25	...	3.00	0.71	0.20	3.47	127
R4	512,256,256	200	26	61.92	9.45	0.17	...	3.59	0.12	0.02	7.36	890
R8	1024,512,512	50	2.8	69.24	9.23	0.14	...	3.98	0.03	0.01	3.17	3671
R1x	128,64,256	800	40	65.15	9.37	0.16	...	3.76	0.90	0.44	2.02	126
R1x24	128,64,256	800	80	45.85	9.50	1.30	0.56	2.68	1.13	0.09	12.8	70
R2x24	256,128,256	600	60	46.90	9.60	1.37	0.58	2.72	0.29	0.03	8.88	278
R4x24	512,256,256	200	20	52.32	9.54	1.34	0.65	3.03	0.09	0.02	3.97	960

Note. Parameters and results of the simulations presented in this work. The angular brackets, $\langle \rangle$, correspond to volume and temporal averages considering only the convection zone, i.e., an average over the radii of the profiles presented in Figures 3, 4, 8, and 9. The Rossby number is defined as $\text{Ro} = P_{\text{rot}}/\tau_c$, where $\tau_c = \ell_c/\langle U \rangle_{\text{rms}}$ is the convective turnover time. For simplicity, the convective correlation length, ℓ_c , is defined as the thickness of the unstable layer. The turbulent viscosity is calculated as $\nu_t = \ell_c \langle U \rangle_{\text{rms}}/3$. Estimates of the effective viscosity, ν_{eff} and κ_{eff} , are computed as described in Appendix B. With these values, the effective Prandtl and Reynolds numbers are computed as $\text{Pr}_{\text{eff}} = \nu_{\text{eff}}/\kappa_{\text{eff}}$, $\text{Re}_{\text{eff}} = \ell_c \langle U \rangle_{\text{rms}}/\nu_{\text{eff}}$.

boundary condition is imposed at their base (e.g., Fan & Fang 2014; Hotta 2018). This is important because it creates a steeper transition between convective and radiative layers.

The averaged values of the perturbations of potential temperature are presented in Figure 3(d). Despite simulations R1 and R2 showing higher values of Θ' at the upper levels, the profiles for models R1x, R4, and R8 are rather similar. The profile of the luminosity, $L_c = 4\pi r^2 F_c$, carried by the enthalpy flux, $F_c = R_g c_p \rho \langle w \Theta' \rangle_{\phi\theta}$, for all nonrotating cases, is shown with solid lines in Figure 4(a). The profiles are normalized to the solar luminosity, L_\odot . Notice that L_c decreases with the increase of resolution, and has a similar profile for simulations R1x and R4. The higher values reached in the low-resolution simulations reflect the strong perturbations of Θ in the upper layers of the domain in Figure 3(d). The profile for case R8 is different, perhaps due to insufficient statistics. The inset of Figure 4(a) shows the bottom of the convection zone where the enthalpy flux is negative. This thin layer, where the correlations between w (mostly negative due to fast downward plumes) and Θ' (positive) are negative, is associated with overshooting. It is roughly zero for case R1, and it increases with the grid size until reaching roughly similar values for the higher-resolution simulations R4 and R8. The luminosity carried by the kinetic energy flux, $L_k = 4\pi r^2 F_k$, with $F_k = \rho \langle w(u^2 + v^2 + w^2) \rangle_{\phi\theta}$ is presented in the same panel with dotted lines. The flux is negative for all cases with minimum values reached by the high-resolution simulations.

3.1.1. Spectral Analysis

In this section, we present the spectral properties of the nonrotating simulations. We are interested in the distribution of energy among convective scales for the different components of the flow. The library SHTns (Schaeffer 2013)⁵ is used to compute the spectral representation of the vector velocity field as

$$\mathbf{u}(\theta, \phi) = \sum_\ell \sum_{m=-\ell}^\ell q_\ell^m \mathbf{Q}_\ell^m(\theta, \phi) + s_\ell^m \mathbf{S}_\ell^m(\theta, \phi) + t_\ell^m \mathbf{T}_\ell^m(\theta, \phi), \quad (7)$$

where

$$\mathbf{Q}_\ell^m = Y_\ell^m \hat{\mathbf{e}}_r, \quad (8)$$

$$\mathbf{S}_\ell^m = r \nabla Y_\ell^m, \quad (9)$$

$$\mathbf{T}_\ell^m = -r \times \nabla Y_\ell^m, \quad (10)$$

and Y_ℓ^m are spherical harmonics of degree ℓ and order m , with $-\ell \leq m \leq \ell$. The coefficients q_ℓ^m , s_ℓ^m , and t_ℓ^m are the radial and transverse components of the velocity vector. Under this decomposition, the spherical harmonic representation of the total kinetic energy as a function of the harmonic degree ℓ is given by

$$\tilde{E}(\ell) = \sum_{m=-\ell}^\ell |q_\ell^m|^2 + \ell(\ell+1)(|s_\ell^m|^2 + |t_\ell^m|^2). \quad (11)$$

The kinetic energy spectra for all nonrotating simulations (see legend in the figure) are presented in Figure 5 for three different depths: (a) $r = 0.95R_\odot$, (b) $r = 0.85R_\odot$, and (c) $r = 0.75R_\odot$. As it could have been anticipated from the results in physical space, as a consequence of poorly resolved motions, simulations R1 and R2 show less kinetic energy at the upper layers and an excess of energy at large wavenumbers. However, simulations R4 and R8 have similar spectra with maximum amplitudes at $\ell \sim 3$. In the middle and bottom of the convection zone, the energy at the largest scales, $\ell < 4$, increases with the resolution. This indicates that the effective viscosity is decreasing and its action shifting toward the smaller scales (see Table 1 and Appendix B). For $\ell \gtrsim 4$, the kinetic spectra of simulations R2-R8 are similar. With the increase of the resolution, the spectra extend over more scales, reaching about two decades of ℓ for R8.

As for the energy cascade from the most energetic scales toward the dissipative scales, the simulations show a scaling slower than the Kolmogorov law, $k^{-5/3}$ (Kolmogorov 1941), especially in the middle and bottom of the convection zone. This result is expected, given the buoyant force in an atmosphere with significant density stratification. Qualitative inspection shows that the Kolmogorov rule seems to exist in small regions of the inertial scale.

A surprising aspect of the figure is the spectra from simulation R1x presented with black dashed lines. Although this case has a coarse horizontal resolution equivalent to R1, as well as a high-resolution equivalent to case R4, only in radius,

⁵ See also <https://www2.atmos.umd.edu/~dkleist/docs/shtns/doc/html/index.html>

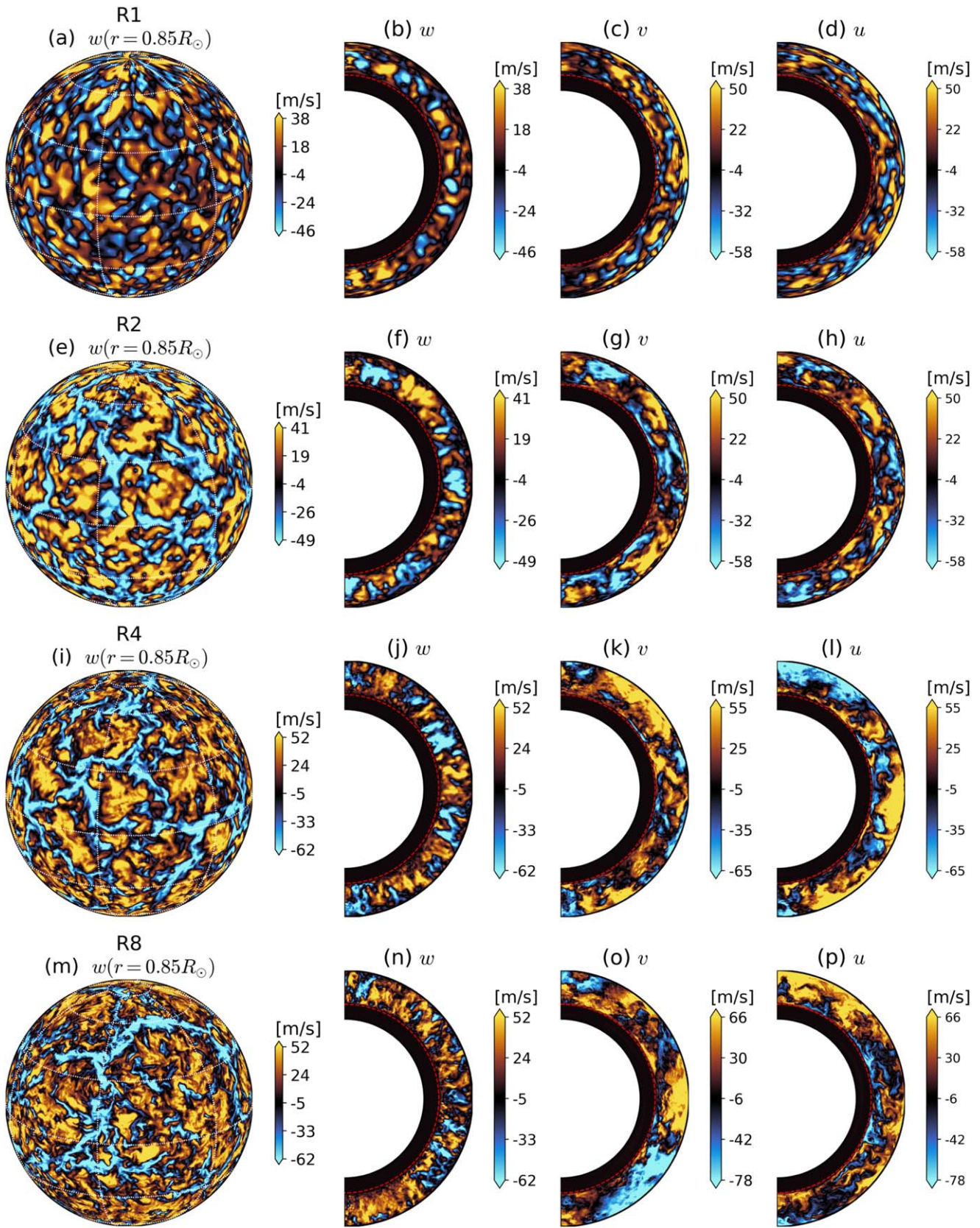


Figure 2. Instantaneous snapshots of the velocity components for simulations R1 to R8, from top to bottom. The radial velocity, w , is presented in the orthographic projection (panels a, e, i, and m) and in the meridional plane (b, f, j, and n). The latitudinal, v (panels c, g, k, and o), and the longitudinal, u (panels d, h, l, and p), components are presented in the meridional plane. The thin dashed red line shows the transition between the stable and unstable layers.

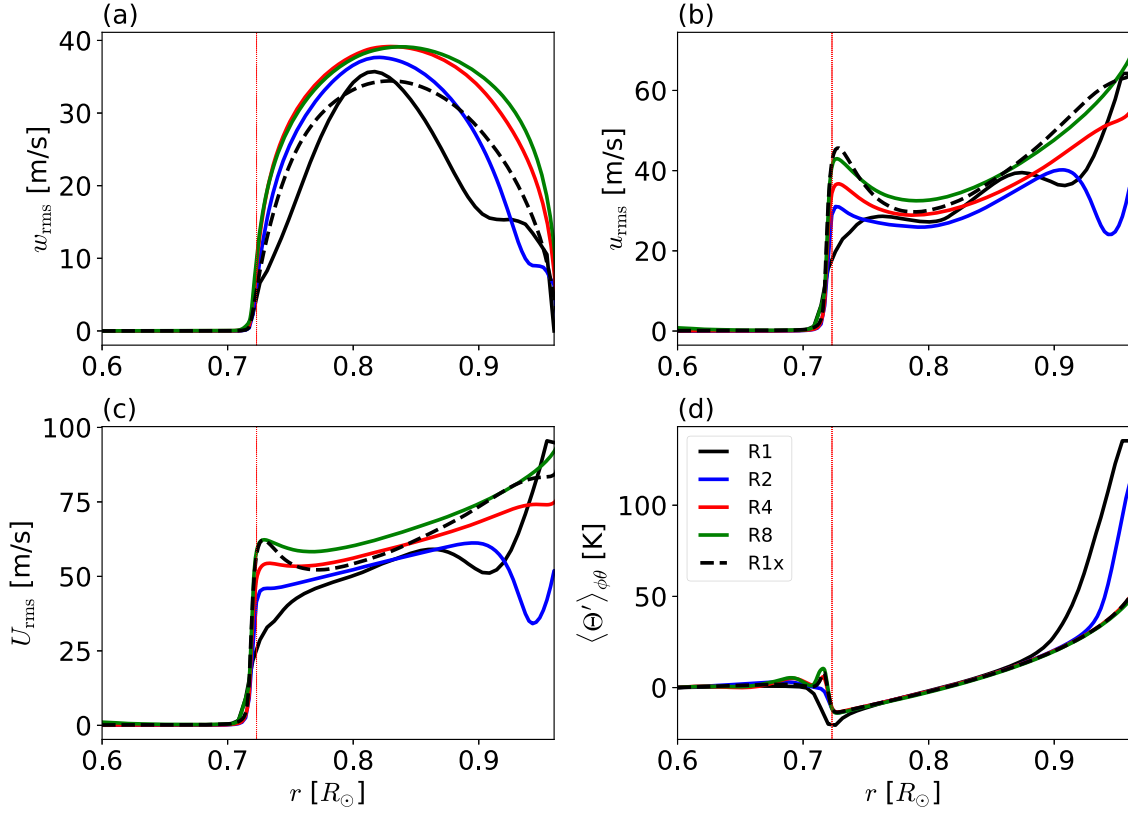


Figure 3. Radial profiles of w_{rms} (a), u_{rms} (b), the total U_{rms} (c), and the perturbations of potential temperature (d). The profile of the latitudinal component v_{rms} is similar to u_{rms} . The averaging was performed in the horizontal directions and time. The thin vertical lines show the bottom of the unstable layer.

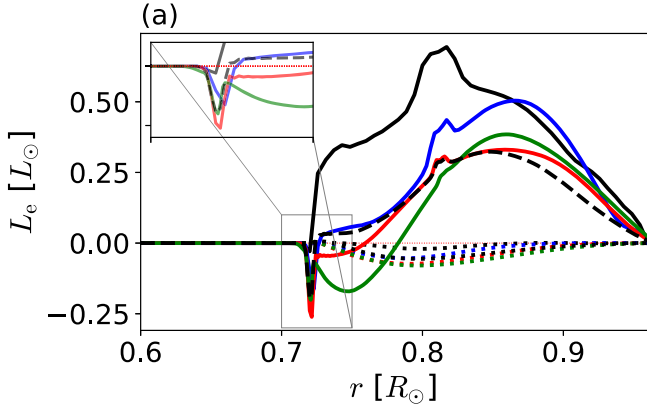


Figure 4. Luminosity carried by the enthalpy flux, $L_e = 4\pi r^2 R_g c_B \rho \langle w \Theta' \rangle_{\phi\theta}$ (solid lines), and the kinetic energy flux, $L_k = 4\pi r^2 \rho \langle w(u^2 + v^2 + w^2) \rangle_{\phi\theta}$ (dotted lines), for the nonrotating simulations presented in Table 1. The color-coding of the lines is the same as in Figure 3. The inset shows the overshooting region with negative values of L_e .

its kinetic power spectra are compatible with the highest-resolution cases. The comparison shows that simulation R1x has an excess of energy in the largest scales. However, the energies at the inertial range, as well as the turbulent scaling, have good agreement with R4 and R8.

To assess the relevance of the present results, we compare them with solar supergranulation motions, which are weakly influenced by rotation. Although their nature is still controversial, recent works point toward a buoyant convective origin (Cossette & Rast 2016; Rincon & Rieutord 2018). Recently, Rincon et al. (2017) developed analytical scaling laws for the spectral behavior of a flow in a stratified

atmosphere in the presence of buoyancy, i.e., anisotropic turbulence. They successfully compared these results with the spectra of supergranulation reconstructed from Doppler and photometric measurements of the Helioseismic and Magnetic (HMI) instrument on board the Solar Dynamics Observatory (SDO) satellite (Scherrer et al. 2012), and decomposed in the spherical harmonic components. This supports the hypothesis that supergranulation is a particular scale of buoyantly driven convection. It is possible to evaluate whether the convectively driven motions developed in the simulations above are comparable with their results.

Figure 6 shows the kinetic energy spectra decomposed into the radial (black lines), spheroidal (blue), and toroidal (yellow) components at $r = 0.95R_\odot$ for simulations R1 (panel a) to R8 (d), as well as R1x (presented in panel c). These components are obtained by separating the terms in the RHS of Equation (11),

$$\begin{aligned} \tilde{E}_Q(\ell) &= \sum_{m=-\ell}^{\ell} |q_\ell^m|^2, \\ \tilde{E}_S(\ell) &= \sum_{m=-\ell}^{\ell} \ell(\ell+1) |s_\ell^m|^2, \\ \tilde{E}_T(\ell) &= \sum_{m=-\ell}^{\ell} \ell(\ell+1) |t_\ell^m|^2. \end{aligned} \quad (12)$$

Under this decomposition, \tilde{E}_S and \tilde{E}_T are measurements of the flow divergence and vorticity in the (ϕ, θ) plane, respectively. In this sense, toroidal does not correspond to the longitudinal component of the flow, as usually assumed in mean-field theory. In this representation, simulations R1 and R2 are strikingly

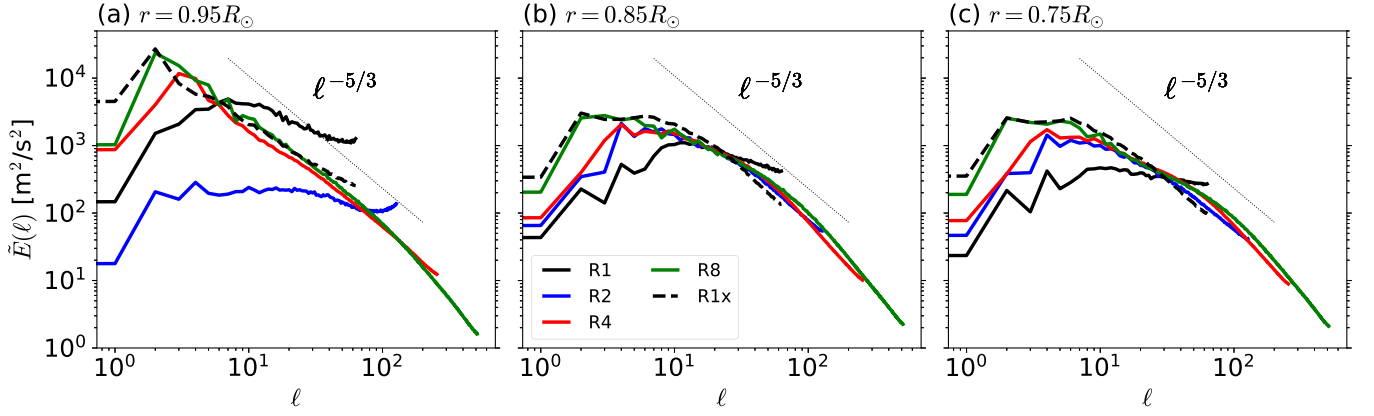


Figure 5. Turbulent kinetic power spectra for simulations with different resolutions R1–R8 (see color correspondence in the legend), at three different depths, from left to right. The black dashed line corresponds to a simulation with the same horizontal resolution as R1 but with 256 grid points in the radial direction. The dotted line shows the $\ell^{-5/3}$ Kolmogorov scaling.

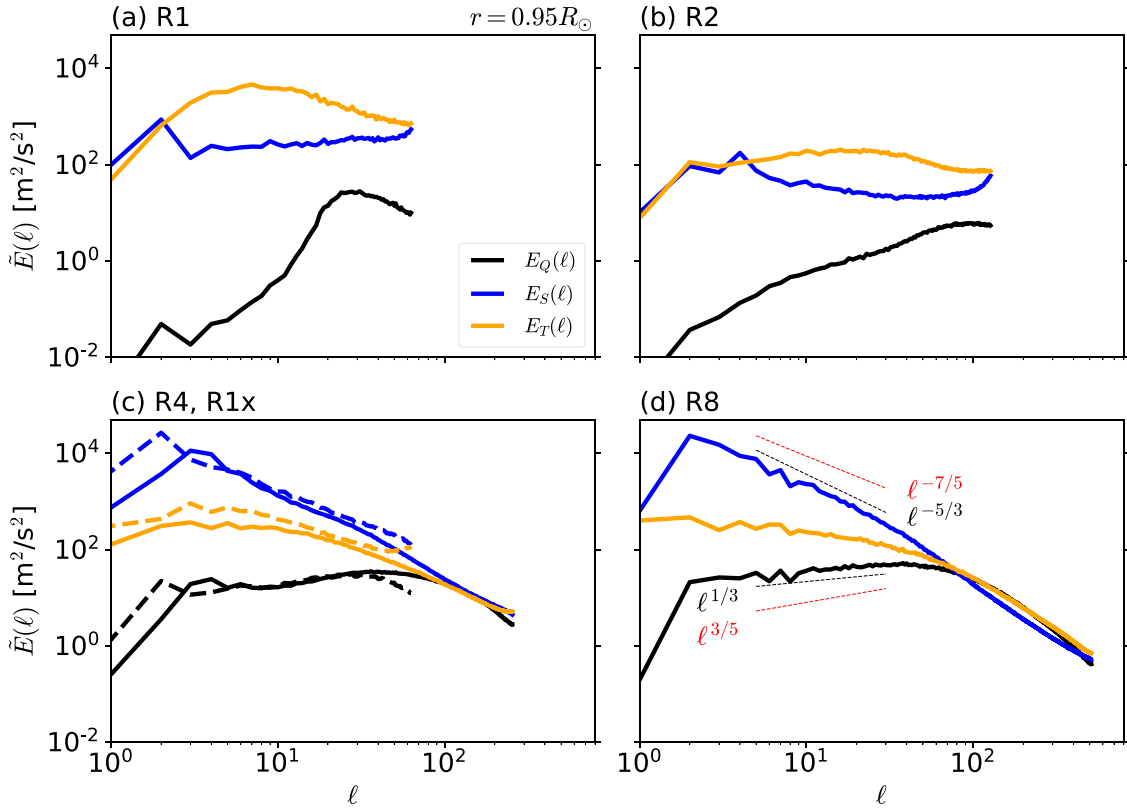


Figure 6. Kinetic power spectra for the spheroidal (blue lines), toroidal (yellow), and radial (black) components of the velocity field at $r = 0.95R_{\odot}$ for simulations (a) R1 to (d) R8. The dashed lines in panel (c) correspond to simulation R1x. The results of panels (c) and (d) indicate strongly anisotropic convection with divergent flows more energetic than the radial flows. The black and red dashed lines in panel (d) show the Kolmogorov (1941) and Rincon et al. (2017) predictions, respectively, for the spectra of turbulent motions.

different from all the others. These simulations have more energy in the toroidal motions than in the radial and spheroidal motions. The distribution of energy changes in simulation R2, but a convergent pattern seems to appear for cases R4 and R8. The results clearly show anisotropic turbulence, with the spheroidal, divergent part of the motions having $\sim 10^3$ times more energy than the radial flows. In panel (c), simulations R4 (continuous lines) and R1x (dashed lines) are compared. Both cases show similar spectral properties. In panel (d), the red dotted lines correspond to the scaling laws for spheroidal and radial motions derived by Rincon et al. (2017). The black dotted

lines correspond to their Kolmogorov equivalents. The scaling laws followed by the motions in our simulations R4, R8, and R1x, which are certainly of buoyant origin, compare well with those of Rincon et al. (2017). However, the Kolmogorov laws are also plausible, and it is hard to distinguish what law is followed and in what spectral range.

Caution is needed in this comparison, because the simulations correspond to a thick shell and develop scales considerably larger than supergranulation (supergranulation has its maximum energy at $\ell \sim 120$, whereas the simulation results show peaks at $\ell \sim 3$). Nevertheless, the energy distribution

among the different components of the velocity, the morphology of the spectral curves, with the spheroidal motion peaking at a large scale, the radial kinetic energy having a kink at the same scale but peaking at a smaller one, and the compatible turbulent scaling laws, demonstrate that simulations R1x, R4, and R8 capture well the properties of convective motions unconstrained by rotation.

It is also worth comparing the findings described above with those of others in similar simulations. The spherical high-resolution simulation, case SD, presented in Hotta et al. (2019), has a radial profile of the rms velocity that is qualitatively similar to the profiles of U_{rms} presented in Figure 3(c). Because in their simulations convection carries almost the entire solar luminosity, the amplitude of the velocity is larger. The turbulent kinetic spectrum of this case has about two orders of magnitude more energy in the horizontal than in the radial motions (see also Hotta et al. 2014). In the cases presented here, the anisotropy is larger, as can be seen in Figures 6(c) and (d). In their spectrum for the horizontal velocity, the maximum is at $\ell \sim 5$ or 6, in fair agreement with our findings.

In the study performed by Featherstone & Hindman (2016a), including low- and high-resolution simulations, the situation is different. Their sets of simulations with density scale heights $N_\rho = 3$ and 4 are compatible with the experiments presented here. Unlike what is observed in Figure 3(a), in their profiles of the rms radial velocity component, the maximum shifts toward the top boundary of the model with the increase of the resolution (accompanied by an increase in the Rayleigh number). In their kinetic spectra, the largest scale, $\ell = 1$, has the maximum power. In their low-resolution simulations, the power at low ℓ 's is larger and decreases for higher resolution, where the newly resolved motions acquire considerable energy. Thus, their inertial range becomes flat. This difference is intriguing. It might arise from the difference in the energy equation between this work and Featherstone & Hindman (2016a). However, both Featherstone & Hindman (2016a) and Hotta et al. (2019) consider somewhat similar energy equations, including a static background state and radiative diffusivity. On the other hand, Featherstone & Hindman (2016a) consider explicit viscous dissipation, whereas in this work and in Hotta et al. (2019), it comes from the numerical scheme.

3.2. Rotating Solar Convection

Here, we present simulations that include the Coriolis force in the momentum equation, Equation (2) (see Table 1). In numerical experiments not presented here, we noticed that the convergence to a steady-state solution occurs faster if the initial conditions are random perturbations rather than the nonrotating relaxed state. Figure 7 depicts the morphological characteristics of the instantaneous radial flow in the orthographic projection at $r = 0.85R_\odot$ (see panels a, e, and i for simulations R1x24, R2x24, and R4x24, respectively), as well as in the meridional plane (panels b, f, and j), along with the latitudinal velocity (panels c, g, and k) and the longitudinal velocity (panels d, h, and l) in the meridional plane.

The orthographic projection shows the elongated structures at equatorial latitudes, also known as ‘‘banana cells,’’ characteristic of rotationally constrained motions taking the form of columns (Busse & Or 1986). For cases R2x24 and R4x24, regions of strongly stretched structures are observed at intermediate latitudes. These are a consequence of the resulting large-scale shear. In the meridional plane, the convective motions at equatorial latitudes are not radial, as in the

nonrotating cases presented in Figure 2; instead, they form elongated convective columns aligned with the rotation axis. At higher latitudes, there are multiple convective cells, exceeding the number in the nonrotating cases, with a certain tilt regarding the rotation axis. The latitudinal velocity (panels c, g, and k) shows flow parcels that are aligned to the rotation axis. The number of these structures seems to increase with the resolution. Finally, the instantaneous snapshot of the longitudinal velocity evinces the sustained large-scale longitudinal flow resulting from each case. The low-resolution case shows an accelerated equator and deceleration toward high latitudes (panel d). The case R2x24 shows a fast rotating equator, a column of retrograde flow above the tangent cylinder, and a column of accelerated motions inside the tangent cylinder (h). In case R4x24, the velocity at the equator diminishes, whereas the higher-latitude acceleration increases and advances toward the poles (l). We discuss the sustainment of this longitudinal mean flow and its coupled meridional flow in Section 3.2.2.

Figure 8 compares the same averaged quantities presented in Figure 3 between the rotating cases, R1x24, R2x24, and R4x24 (blue, red, and green lines, respectively). For comparison, the results for the nonrotating models R1x and R4 are presented in black and gray dotted lines, respectively. It is expected that the amplitude of the velocity field components is quenched by the Coriolis force. This change is evident by comparing the continuous color lines with the dotted dark lines. For simulations R1x24 and R4x24, the mean radial velocity, w_{rms} , is $\sim 65\%$ and $\sim 70\%$ of the values for the cases R1x and R4, respectively (panel a). Most important for this paper is the observed trend of this quantity to acquire larger values with the increase of numerical resolution. Note also that the maximum of w_{rms} moves toward the upper boundary. The longitudinal component, u_{rms} (b), also decreases compared to the models without rotation, but the change is not as significant as for w_{rms} . It is noteworthy that the rms horizontal motions slightly penetrate into the stable layer at $r \sim 0.7R_\odot$ (see vertical red line), and even at deeper layers there is a nonzero velocity. This nonvanishing velocity suggests a weak level of turbulence in the stable layer. It may be a byproduct of shear instabilities, inertial waves driven by the Coriolis force, or internal gravity waves. The perturbations of Θ (panel d) do not show significant changes in the convection zone with respect to the nonrotating cases. Also, there are no notable differences between simulations with different resolutions. However, at the bottom of the CZ, there is a valley of negative perturbations that is deeper for higher resolution. A positive peak can be identified slightly below the CZ. Its location is roughly the same for all rotating cases. As seen below, these maxima appear as a consequence of the large-scale shear that establishes at the tachocline and their associated thermal wind balance.

The luminosity carried by the enthalpy flux resulting in the rotating simulations is presented in Figure 9. It is interesting that, despite the differences in w_{rms} between simulations R1x24 to R4x24, the average of the correlations $w_{\text{rms}}\Theta'$ remains roughly the same for all cases, carrying approximately 25% of the solar luminosity. Also, despite the fact that rotation causes w_{rms} to peak closer to the top of the domain, the maxima of L_e is shifted downward, with respect to the nonrotating cases (for comparison, see the black dotted lines in the figure, corresponding to simulations R1x and R4). The figure also shows that rotation diminishes overshooting. The bottom of the convection zone is focused in the inset in the figure. It clearly

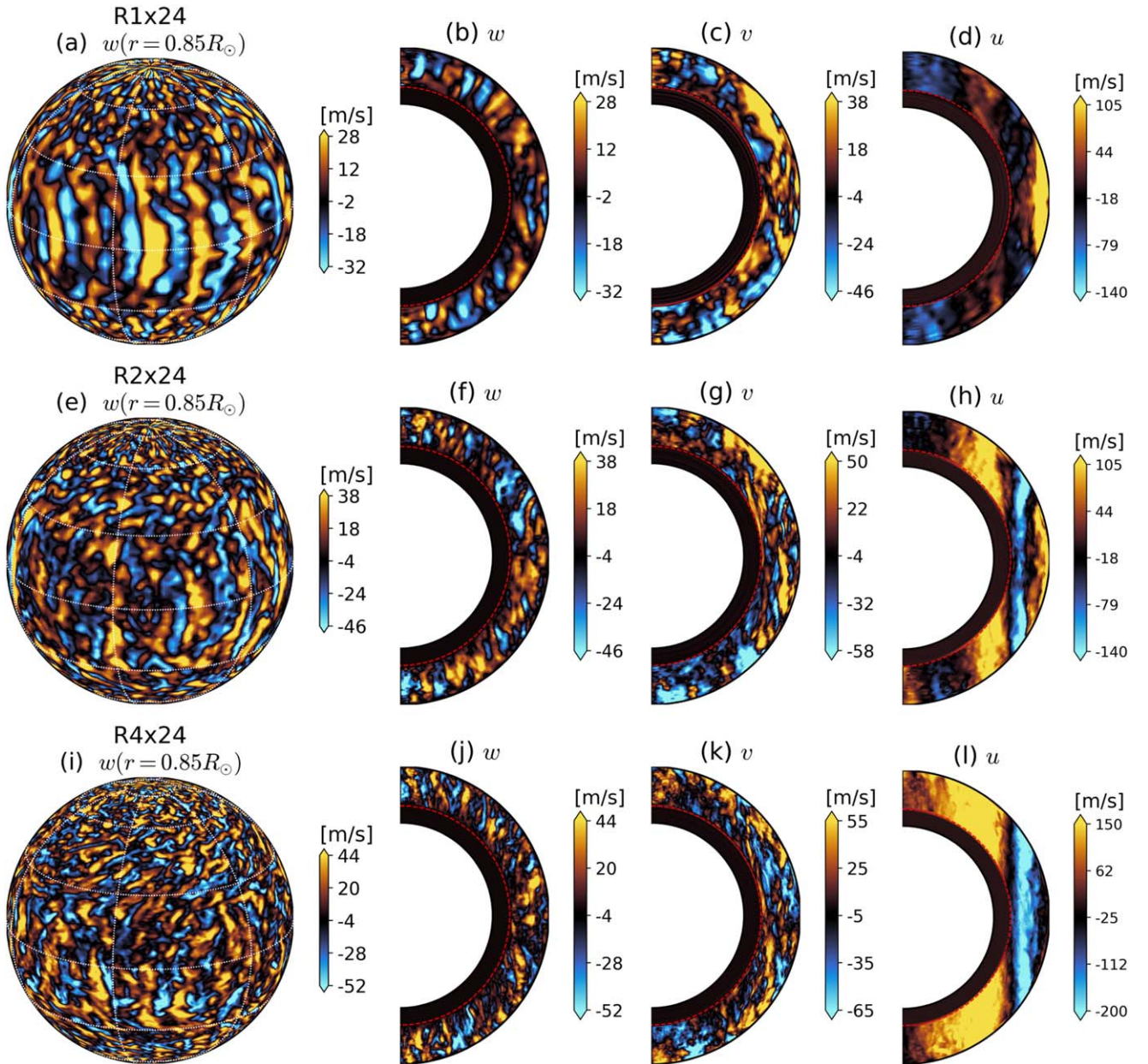


Figure 7. Same as Figure 2, but for simulations R1x24, R2x24, and R4x24, from top to bottom.

shows a considerable difference between the nonrotating cases, presented in dashed dark lines, and the rotating simulations. Finally, the dotted lines in the figures show the luminosity carried by the kinetic energy flux. It is evident that it is much smaller than in the nonrotating cases. Therefore, the luminosity carried by convection—see the residual between L_e and L_k —is mostly due to the enthalpy flux.

3.2.1. Spectral Analysis

The turbulent kinetic energy spectra of the rotating simulations at different depths are presented in Figures 10(a)–(c). In this figure, only the decomposition in the \tilde{E}_Q (black line), \tilde{E}_S (blue), and \tilde{E}_T (yellow) components (Equation (12)) is presented. The full kinetic spectra (Equation (11)) follow the curves of the most energetic component—in this case, the toroidal kinetic energy. Note also that these spectra correspond to the turbulent velocity field, removing the axisymmetric

component, $m=0$, from the total velocity vector, i.e., $\mathbf{u}' = \mathbf{u} - \bar{\mathbf{u}}$. The thick dashed, dotted, and solid lines correspond to cases R1x24, R2x24, and R4x24, respectively. The spectra for the nonrotating case R4 are presented in thin continuous lines for comparison. For rotating convection, the spectra reveal anisotropic motions. This time, however, the toroidal component is the dominant one. The radial velocity is the less energetic component. The anisotropy is more pronounced near the top of the model domain, with an energy difference of about two orders of magnitude at the scales of the most energetic motions. In the middle and bottom of the CZ, the anisotropy diminishes and the energy difference is about a factor of two.

As a consequence of the Coriolis force, the broad convective cells observed for nonrotating convection, with maximum energy at the harmonic degree $\ell \sim 3$, are broken into cells with scales peaking at $\ell \sim 30$ at the upper part of the domain and

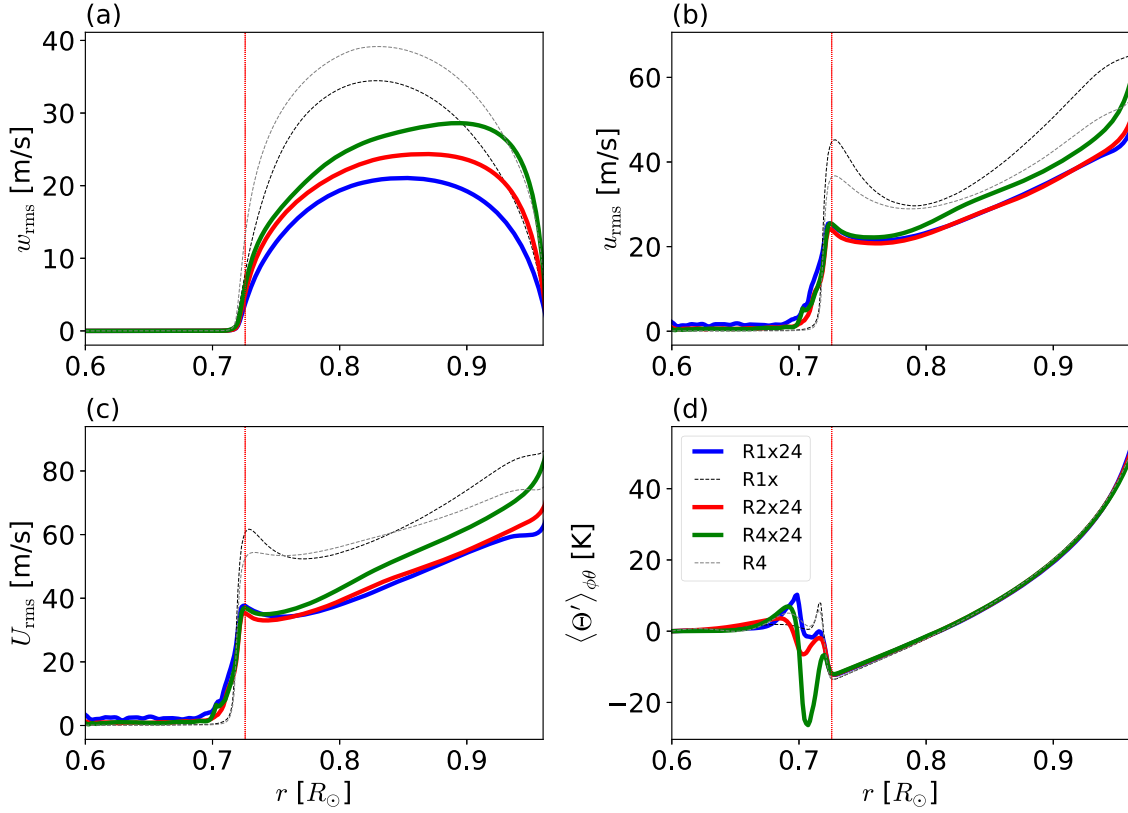


Figure 8. Same as Figure 3, but for the rotating simulations with different resolutions, R1x24 (blue), R2x24 (red), and R4x24 (green). For comparison, the profiles corresponding to the nonrotating cases R1x and R4 are presented with black and gray dotted lines, respectively. The thin red vertical lines show the bottom of the convection zone.

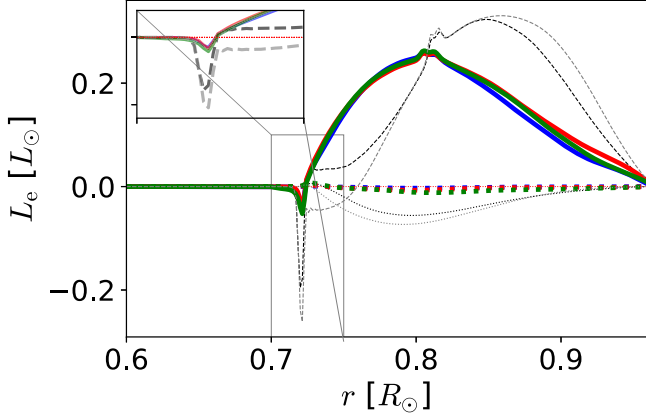


Figure 9. Luminosity carried by the enthalpy flux in the rotating simulations R1x24, R2x24, and R4x24. For comparison to the nonrotating cases, the dotted black and gray lines correspond to simulations R1x and R4, respectively. The inset focuses on the bottom of the convection zone and shows that overshooting decreases because of rotation. The dotted lines show the luminosity carried by the kinetic energy flux.

with most of the energy in \tilde{E}_T . At the middle and bottom, there are peaks of energy at values of ℓ between 6 and 8.

It has been reported in both HD (Featherstone & Hindman 2016b) and MHD simulations (Guerrero et al. 2019) that the spatial scale where the spectra peak depends on the Rossby number. The results presented in this study show that the Rossby number also changes with the numerical resolution. However, a shift in the spatial scale of the energy peak is observed only for the radial component at the domain’s surface (panel a). \tilde{E}_Q peaks at $\ell \sim 30$ for simulation R1x24, $\ell \sim 40$ for

simulation R2x24, and $\ell \sim 50$ for case R4x24. Concurrently, the energy increases by a factor of two to three between the low- and the highest-resolution cases. In the Sun, the radial spectral energy has a maximum at $\ell \sim 400$ for supergranular motions. Yet, as previously mentioned, supergranules are mainly divergent motions with most of the energy contained in the spheroidal energy component. Interestingly, a relevant change in the energy-containing scale of the horizontal velocity components with the mesh size is not observed. It is worth remembering here that the longitudinal velocity, which largely contributes to \tilde{E}_T , is the component used for measuring the observational spectra (Proxauf 2020). At large values of ℓ , the spectra decay with a scaling law faster than the Kolmogorov $\ell^{-5/3}$ rule at all depths (see the thin dotted lines). It is a remarkable result that the spectra do not show dramatic changes with the resolution except the one described for \tilde{E}_Q at upper radial levels. Surprisingly, the large-scale patterns deriving from these turbulent flows result in fully divergent outcomes, as will be presented below.

It is illuminating to compare these findings with the results of the high-resolution rotating simulation performed by Miesch et al. (2008). Their kinetic spectra show anisotropic motions at surface levels with the maxima energy in the horizontal velocity components and at the harmonic degrees $\ell = 20 - 30$. The spectrum of the radial velocity component peaks at $\ell = 80$. Below the model’s top boundary, the motions become more isotropic. These results are generally in good agreement with those presented in Figure 10, i.e., with the increase of resolution, the radial velocity shifts to larger energy and smaller scales. On the other hand, the

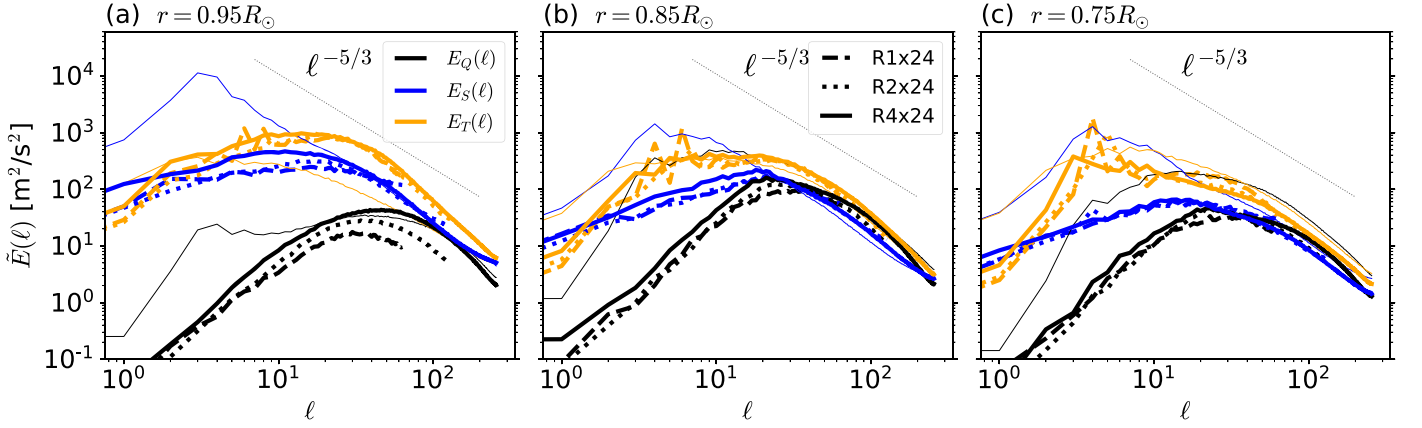


Figure 10. Same as Figure 6, but for simulations R1x24 (dashed line), R2x24 (dotted), and R1_24 (solid). Note that the peak of the spectra of the rotating simulation is shifted toward the smaller scales, $\ell \sim 40$. Moreover, increasing resolution leads to larger power in the radial component, with the maximum being shifted to the smaller scales. For comparison, the thin solid lines show the spectra of case R4 at the corresponding depths.

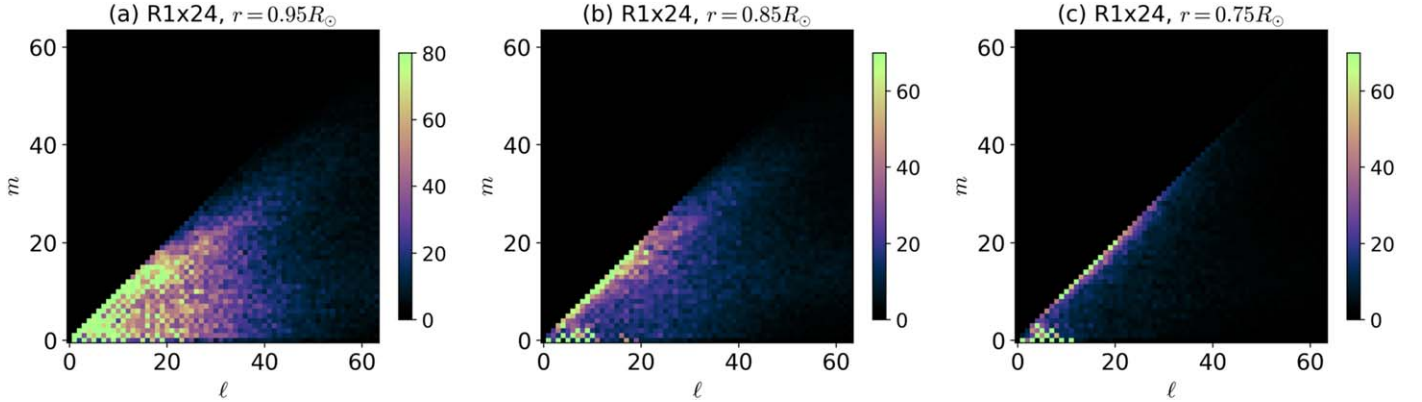


Figure 11. Two-dimensional kinetic energy spectra for simulation R1x24 at the top (a), middle (b), and bottom (c) of the domain. The bottom left points observed in panels (b) and (c) correspond to inertial modes driven by the Coriolis force.

spectra of the horizontal components seem to be independent of the resolution. Nonetheless, despite the agreement in the spectral properties, the resulting mean flows of simulation R4x24 differ from their findings (see Figure 6 of Miesch et al. 2008).

From the graphs presented in Figure 10, the maxima appearing between $6 \lesssim \ell \lesssim 10$ stand out. They are more evident at the middle and the bottom of the domain; see Figures 10(b) and (c). As a matter of fact, these peaks contain the largest energy at the bottom of the CZ. To identify to what motions these peaks correspond, Figure 11 presents two-dimensional spectra for the simulation R1x24. These spectra are computed using Equation (11) but not considering the sum over m and averaging only over time. Panels (b) and (c) reveal that the high-energy harmonics in this particular range correspond to low-order longitudinal modes, $m = 1$ to 4. These are inertial modes, similar to Rossby waves, developing below the convection zone. It is observed that their maximal energy is at depth $r = 0.71R_\odot$, and quite remarkably, these peaks appear at the same scales independently of the resolution. Because of their energy, which seems to propagate upward to higher radial levels, these modes are likely to be dynamically important in the rotating convective system. Assessing the properties of these waves and their relevance is left for an independent study (Dias et al., in preparation).

The banana cells, clearly observed in Figures 7(a), (e), and (i) at $r = 0.85R_\odot$, have longitudinal wavenumbers $16 < m < 20$; therefore, in the (m, ℓ) plane, they are close to the diagonal in Figure 11(b). At the top of the domain, the 2D spectrum shows large energies in the diagonal but also below it. The analysis of solar motions by Getling & Kosovichev (2022) presents similar 2D spectra. At the deepest layers reached by their measurements, 19 Mm below the solar surface, their spectrum shows higher energy levels below the diagonal, with scales peaking between $10 \lesssim \ell \lesssim 40$. The results presented in Figure 11(a) resemble these observations.

3.2.2. Mean Flows and Angular Momentum Transport

Turbulent inverse cascade effects allow the development of large-scale motions with spatial scales of the size of the system and temporal variations much longer than the convective turnover time. These motions can be separated into the longitudinal and meridional components, namely the differential rotation and meridional flow. The resulting differential rotation for simulation R1x24 is solar-like, and is accelerated (decelerated) at the equator (poles) with respect to the frame rotation rate Ω_0 ; see Figures 12(a) and (b). Yet, unlike the Sun, where isorotation contours are conical, the profile has contours that are roughly cylindrical, aligned with the rotation axes.

The ambient state prevents the turbulent motions from penetrating into the stable layer below the thin overshooting region. Thus, a tachocline is formed at the transition between the radiative and convective zones. In the Sun, the tachocline is subjected to radiative spreading (Spiegel & Zahn 1992), and there is not yet widespread agreement with regard to the mechanisms that sustain its thickness. In most simulations including a subadiabatic layer below the convection zone, the tachocline spreads over time due to the imposed viscosity. In the ILES simulations presented here, there is no measurable viscous spreading of the tachocline in the stable layer during the timescale of the simulations. This allows us to assess the role of this layer on the formation and sustainability of large-scale flows.

The meridional circulation is represented in Figure 12(c) through the mean latitudinal velocity in the meridional plane. In the northern hemisphere, the negative (positive) values of \bar{v} correspond to poleward (equatorward) motions. The graph shows several circulation cells appearing at latitudes between $\pm 35^\circ$ with amplitudes of a few m s^{-1} , with the most prominent cells corresponding to clockwise circulation. At higher latitudes, the meridional flow weakly reaches the poles at the upper layers and returns at deeper layers.

The DR of simulation R2x24, illustrated in Figures 12(d) and (e), still shows a fast equator. Nevertheless, a column of strong retrograde velocity appears outside the cylinder tangential to the model's tachocline. Physically, this is an expected outcome if the velocity of counterclockwise convective Busse columns is enhanced due to a large Rossby number (see, e.g., Featherstone & Miesch 2015). Inside the tangent cylinder, there is a column of rotation with roughly the same speed as the equator and slower poles at the highest latitudes. The same characteristics appear in simulation R4x24; however, increasing the resolution further decreases the equatorial speed and enhances the acceleration of the poles. A similar transition was observed by Hindman et al. (2020) for simulations with the same rotation rate and increased Rayleigh and Reynolds numbers. The profiles of meridional flow remain similar in these simulations, yet with stronger meridional flow velocities at intermediate to high latitudes. These enhanced meridional flows transport angular momentum toward the higher latitudes and explain the obtained polar acceleration. In cases R2x24 and R4x24, there are negative and positive radial gradients of $\bar{\Omega}$ at the equator and middle latitudes. Thus, the meridional circulation continues to be multicellular despite the accelerated poles.

Even though a solution independent of the grid resolution is not observed, and the highest-resolution simulation is the farthest from the solar-like rotation, with the data at hand, it is possible to explore the redistribution of angular momentum as a function of the resolution to get a better understanding of the processes that drive and sustain the mean-flow profiles.

The mean angular momentum, $\mathcal{L} = \varpi \rho_r \bar{u}$, where $\varpi = r \sin \theta$ is the lever arm and \bar{u} is the time and longitudinal average of u , evolves according to

$$\frac{\partial \mathcal{L}}{\partial t} = -\nabla \cdot (\varpi [\rho_r (\bar{u} + \varpi \Omega_0) \bar{\mathbf{u}}_m + \rho_r \overline{u' \mathbf{u}'_m}]), \quad (13)$$

where, $\bar{\mathbf{u}}_m$, and \mathbf{u}'_m are the mean and turbulent meridional (r and θ) components of the velocity field, respectively. More explicitly, the terms inside the divergence are the fluxes of

angular momentum,

$$\begin{aligned} \mathcal{F}_r^{\text{RS}} &= \rho_r \overline{\varpi u' w'}, \\ \mathcal{F}_\theta^{\text{RS}} &= \rho_r \overline{\varpi u' v'}, \\ \mathcal{F}_r^{\text{MC}} &= \rho_r \varpi (\bar{u} + \varpi \Omega_0) \bar{w}, \\ \mathcal{F}_\theta^{\text{MC}} &= \rho_r \varpi (\bar{u} + \varpi \Omega_0) \bar{v}, \end{aligned} \quad (14)$$

which arise from the small-scale correlations, i.e., Reynolds stresses (RS), of the turbulent flow (for completeness, the profiles of the RS in the meridional plane for the three rotating simulations are presented in Appendix A) and from the mean profiles of DR and MC in a statistically steady state. It is expected that, during this stage, the LHS of the equation vanishes; therefore, the four fluxes of Equation (14) should balance with each other. The net radial and latitudinal angular momentum transport may be estimated by computing the fluxes across spherical and conical surfaces, respectively (see Brun & Toomre 2002), as

$$\begin{aligned} I_r(r) &= \int_0^\pi \mathcal{F}_r(r, \theta) r^2 \sin \theta d\theta \\ I_\theta(\theta) &= \int_{r_b}^{r_t} \mathcal{F}_\theta(r, \theta) r \sin \theta dr, \end{aligned} \quad (15)$$

where

$$\begin{aligned} \mathcal{F}_r &= \mathcal{F}_r^{\text{MC}} + \mathcal{F}_r^{\text{RS}} \\ \mathcal{F}_\theta &= \mathcal{F}_\theta^{\text{MC}} + \mathcal{F}_\theta^{\text{RS}}. \end{aligned} \quad (16)$$

Since r runs from bottom to top, positive (negative) values of I_r correspond to upward (downward) angular momentum flux. Similarly, θ runs from the north to the south poles; thus, positive (negative) I_θ corresponds to equatorward (poleward) flux in the northern hemisphere. The fluxes of angular momentum for the simulations R1x24, R2x24, and R4x24, integrated over radius and latitude, are presented in the top and bottom rows of Figure 13, panels (a) to (c), respectively. For evaluation of the independent contributions of the RS and the MC, the integrals for $\mathcal{F}_r^{\text{MC}}$ and $\mathcal{F}_\theta^{\text{MC}}$ (red lines), and $\mathcal{F}_r^{\text{RS}}$ and $\mathcal{F}_\theta^{\text{RS}}$ (blue lines) are presented separately. The black dashed lines show the sum of the MC and RS contributions.

For the lowest-resolution case, panel (a), the RS transports angular momentum downward at the bottom half of the convection zone and upward at the upper half. Increasing the resolution leads to an increase in the radial flux (panels b and c). However, for cases R2x24 and R4x24, the RS flux is negative (inward) in most of the convection zone, with boundary regions of positive (upward) flux at the bottom and top of the domain. The radial RS flux is well-balanced by the MC flux, and the sum of the two fluxes is roughly consistent with zero.

The amplitude of the latitudinal fluxes also increases with the numerical resolution. In all of the cases, the RS flux pumps angular momentum toward the equator. Unlike the radial flux, the MC flux does not balance its turbulent counterpart, and it even shows a different profile for each case. In simulation R1x24, I_θ^{MC} has the same sign as I_θ^{RS} at low and intermediate latitudes. Therefore, the net transport of angular momentum is equatorward. This explains the solar-like profile observed in Figures 12(a) and (b). The black dashed line in the bottom panel of Figure 13(a) clearly shows that the two fluxes do not balance each other. In these hydrodynamic simulations, the only term missing in Equation (13) is the molecular viscous

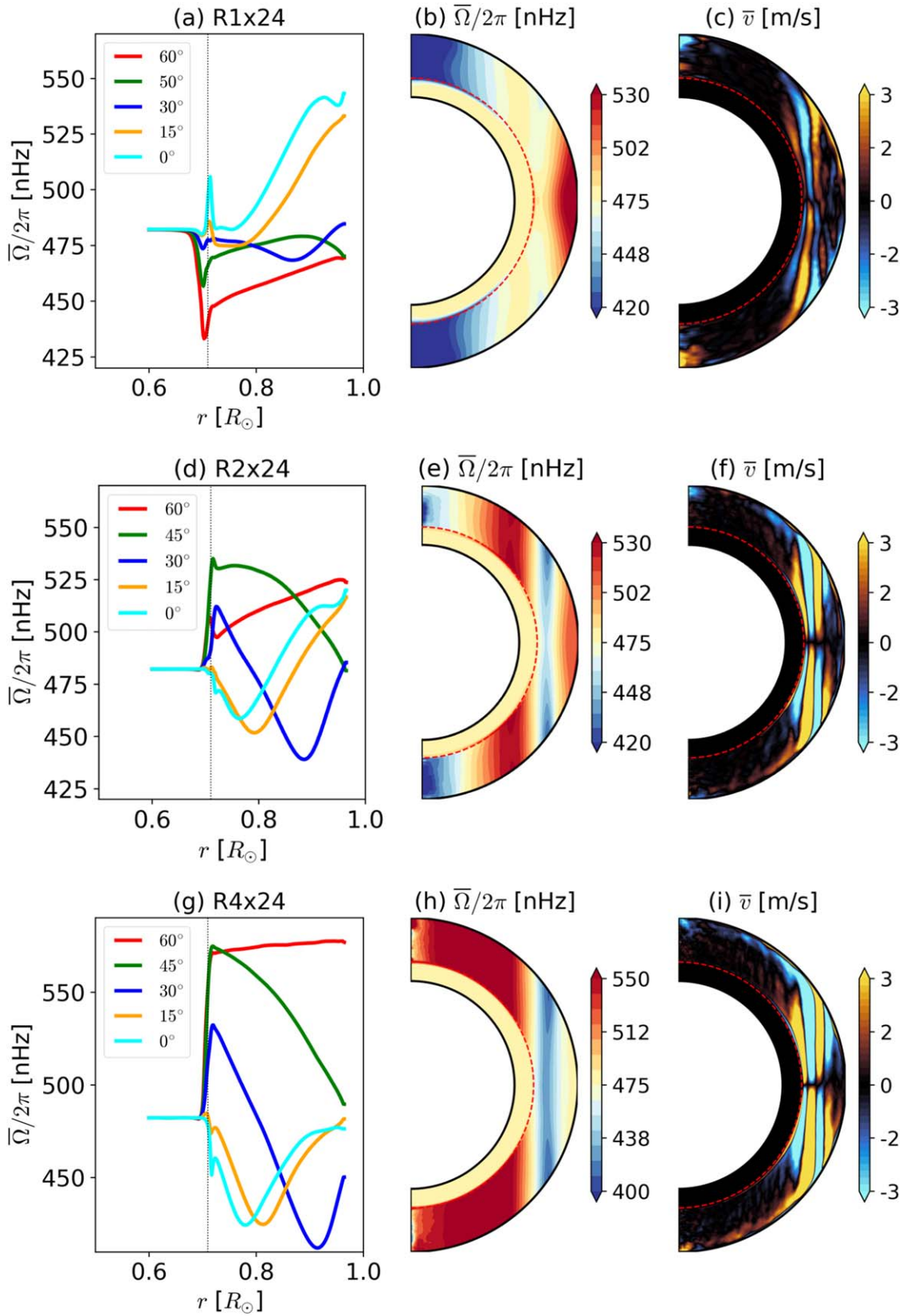


Figure 12. Left and middle panels: differential rotation as a function of radius for different latitudes and in the meridional plane, respectively, for simulations R1x24, R2x24, and R4x24, from top to bottom. Right panels: mean profile of the latitudinal velocity in the meridional plane. In the northern hemisphere, negative (positive) values correspond to poleward (equatorward) flows.

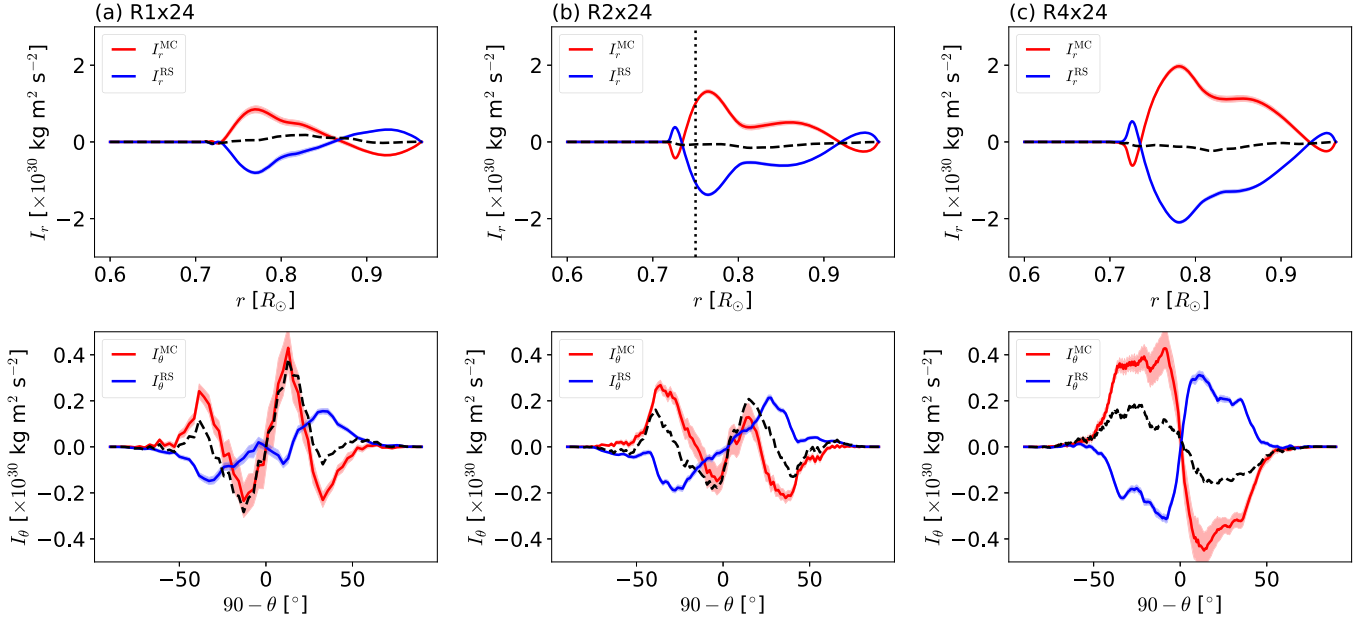


Figure 13. Angular momentum fluxes integrated over spherical surfaces at different r (upper panels) and conical surfaces at latitudes $90 - \theta$ (bottom), for simulations (a) R1x24, (b) R2x24, and (c) R4x24. The red and blue lines correspond to the MS and RS contributions; the dashed black line is the sum of both contributions.

flux. While in the Sun this term must be irrelevant, in the low-resolution case, it appears in the form of effective viscosity. This numerical contribution results in an angular momentum flux with values compatible with the RS and MC fluxes.

In simulations R2x24 and R4x24, the balance between RS and MC fluxes is better, as evidenced by the smaller values reached by the black dashed line relative to the values of I_θ^{RS} and I_θ^{MC} . Yet the balance is not perfect (bottom row of panels b and c). The MC flux assumes the opposite sign of RS and advects angular momentum toward the poles. Notice that, in these three cases, the resolution increases only in the horizontal direction. The estimated values of the effective viscosity presented in Appendix B show that, for the rotating cases, ν_{eff} scales as $N_\phi^{-1.8}$. Thus, changing N_ϕ and N_θ by respective factors of two and four results in changes in the effective viscosity with respective factors of ~ 3 and ~ 11 (see Table 1). It is good to bear in mind, however, that this viscosity is nonlinear and nonhomogeneous, being larger in regions where the flow has steeper variations. The bottom row of Figure 13(c) demonstrates the weaker influence of the effective viscosity on the angular momentum dynamics. In this case, I_θ^{MC} has almost twice the amplitude of I_θ^{RS} . Therefore, the sum of the two also has half of the amplitude of I_θ^{MC} and its contribution aims to settle the balance. The profiles of I_θ^{MC} explain the transition of the DR from the accelerated equator to the accelerated poles. It is worth mentioning here that the profiles in Figure 13(c) are compatible with those of Miesch et al. (2008), with the exception of an enhanced MC latitudinal flux in case R4x24. Nevertheless, unlike the differential rotation profile observed in Figures 12(g) and (h), they obtain a solar-like rotation. There are several differences between the two modeling approaches. The more relevant ones are perhaps the different values of the Prandtl number (0.25 in their case and estimated to be ~ 3 in this work) and the initial condition of the simulation as well as the total evolution time. They enforce a solar-like profile and then evolve the simulation for ~ 3 yr, whereas the models presented here start from random thermal fluctuations and evolve the system for 20 yr.

The large-scale flows observed in Figure 12 are sustained by the fluctuations around average values of the angular momentum fluxes. The shadows around the profiles presented in Figure 13 depict the standard error, $\sigma_e = \sigma/\sqrt{n}$, where σ is the variance and n is the number of samples in the average. It is clear from the figure that the MC flux has larger deviations from the mean profile and that these deviations increase for higher resolutions. This result is not surprising, given the smaller viscous friction that the flow experiences in the higher-resolution cases. The fluctuations are sustained by turbulent convection driven by the buoyancy force. Therefore, Equation (13) does not entirely describe the sustainability of the mean flows.

Before providing an overview of the sustainment of the DR and MC, it is illustrative to compute the divergence of the fluxes on the RHS of Equation (13). Including the minus sign in front, the results are the axial torques,

$$\mathcal{T}^{\text{RS}} = -\frac{1}{r^2} \frac{\partial(r^2 \mathcal{F}_r^{\text{RS}})}{\partial r} - \frac{1}{r \sin \theta} \frac{\partial(\mathcal{F}_\theta^{\text{RS}} \sin \theta)}{\partial \theta}, \quad (17)$$

$$\mathcal{T}^{\text{MC}} = -\frac{1}{r^2} \frac{\partial(r^2 \mathcal{F}_r^{\text{MC}})}{\partial r} - \frac{1}{r \sin \theta} \frac{\partial(\mathcal{F}_\theta^{\text{MC}} \sin \theta)}{\partial \theta}, \quad (18)$$

due to the RS and the MC, respectively. These quantities are presented in Figure 14.

On average, in the steady state, the RS produce a torque that changes sign with radius and latitude. The profiles from simulations R1x24 to R4x24 are similar, although for the higher-resolution cases, the torque becomes stronger and better-aligned with the axis outside the tangent cylinder, and it also seems to reach higher latitudes. To balance these torques, the meridional motions form closed loops with circulations that have axial torques in the direction opposite to that of the RS. This process is called gyroscopic pumping. It is sustained by deviations of the thermal wind balance, as will be seen in the following section. The direction of the meridional flows may be identified by writing Equation (13),

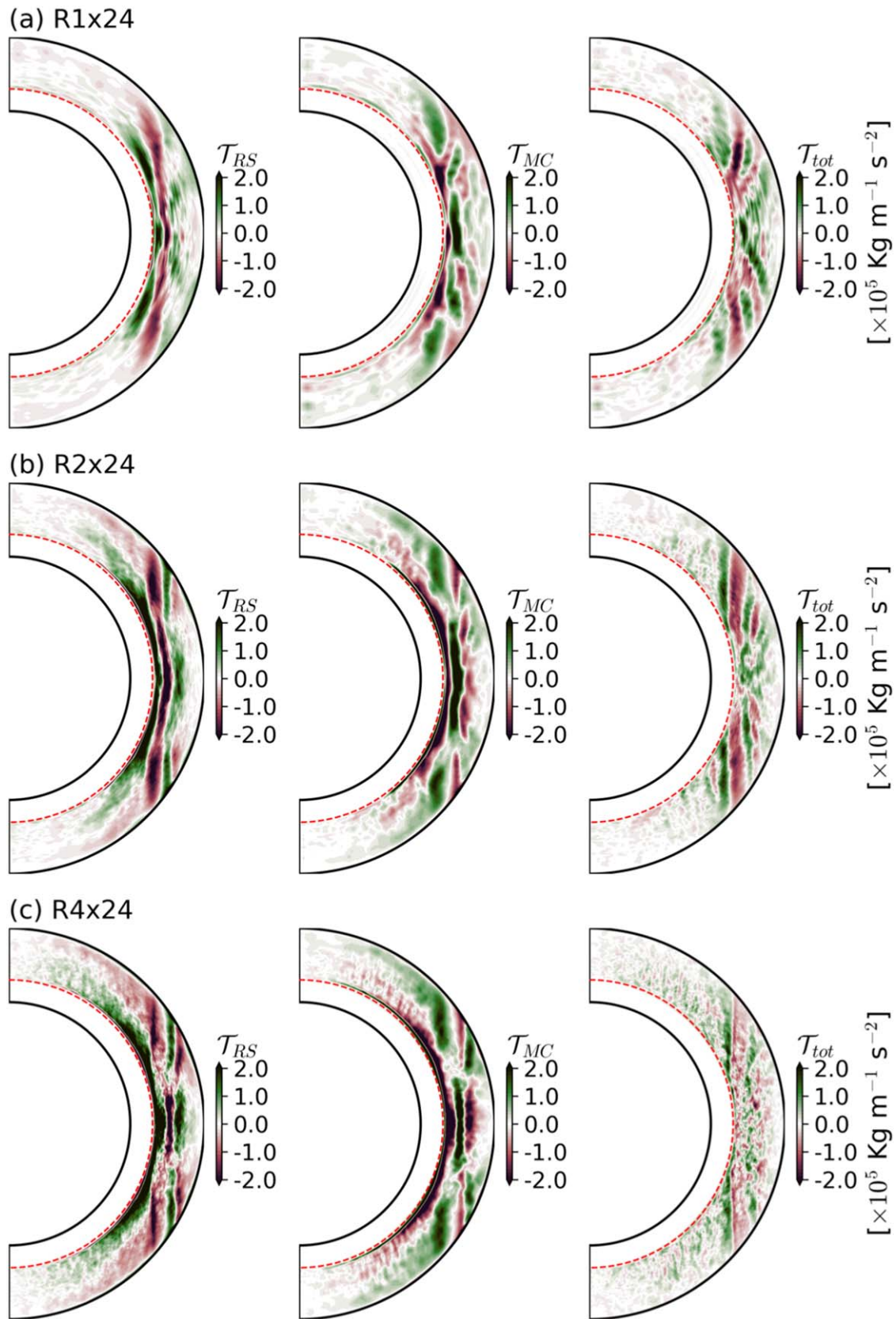


Figure 14. Axial torques due to the RS (left column) and the MC (middle), and the sum of the RS and MC (right) torques, presented in the meridional plane for simulations R1x12 (top row), R2x24 (middle), and R4x24 (bottom).

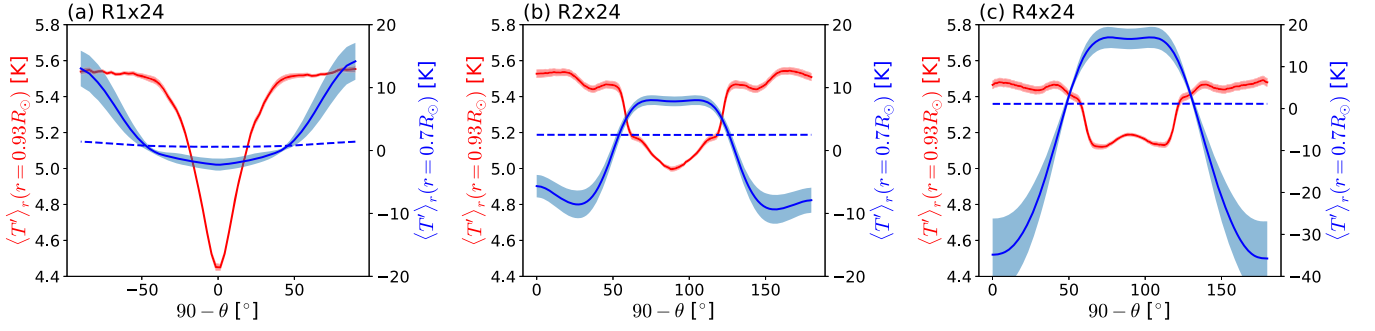


Figure 15. Latitudinal variations of temperature perturbations: the red and blue lines correspond to profiles of temperature perturbations at the surface and the bottom of the convection zone for the models (a) R1x24, (b) R2x24, and (c) R4x24. The contrast at the two radial levels is different; therefore, two different scales at the left and right Y-axis are considered. The dashed line shows a third radial level at $r = 0.66$, where perturbations are not expected. The angled brackets, $\langle \rangle_r$, indicate the radial average centered in $r = 0.71R_\odot$ and $r = 0.93R_\odot$ in a radial layer of thickness $0.04R_\odot$.

with $\partial\mathcal{L}/\partial t = 0$, as

$$\rho_r \bar{\mathbf{u}}_m \cdot \nabla(\varpi^2 \Omega) = -\nabla \cdot (\rho_r \varpi \overline{\mathbf{u}}_m u') = -\mathcal{T}^{\text{RS}}, \quad (19)$$

and with the known profiles of Ω and \mathcal{T}^{RS} (Figures 12 and 14). As a simple example, let us consider the simulation R4x24, with constant θ at the equator, Equation (19) becomes

$$\rho_r \bar{w}_{eq}(r) \frac{\partial}{\partial r}(r^2 \Omega_{eq}(r)) = -\frac{1}{r^2} \frac{\partial}{\partial r}(r^2 \mathcal{F}_{r,eq}^{\text{RS}}(r)). \quad (20)$$

The radial derivative at the LHS is positive for all r , whereas the radial derivative at the RHS changes sign several times. It is negative for $0.72R_\odot \lesssim r \lesssim 0.77$, positive for $0.77R_\odot \lesssim r \lesssim 0.82$, and negative again for $0.82R_\odot \lesssim r \lesssim 0.9$, from which point on it is positive; see the leftmost panel of Figure 14(c). Thus, because of the minus sign in the RHS, the profile of $\bar{w}_{eq}(r)$ has to have the sign opposite to that of $\frac{\partial}{\partial r}(r^2 \mathcal{F}_{r,eq}^{\text{RS}}(r))$. We have numerically verified that this relation is obeyed for all values of r .

Figure 14 shows that the MC torque has roughly the same profile as the RS torque, yet with the opposite sign. The third column of the figure depicts $\mathcal{T}_{\text{tot}} = \mathcal{T}^{\text{RS}} + \mathcal{T}^{\text{MC}}$. It shows that the balance is not perfect, suggesting the contribution of axial torques by the effective viscosity. With the increase of the resolution, shown in panels (a) to (c), the values of the axial torques become higher, the balance seems to improve, and \mathcal{T}_{tot} is evidently less coherent. Both changes are a consequence of the diminished viscous resistance to turbulent motions.

3.2.3. Differential Temperature and Thermal Wind Balance

Both quantities on the LHS of Equation (19) are sustained from the departures of the equilibrium state through fluctuations driven by convection, which in turn is sustained by the buoyancy force. An equation including this contribution may be obtained by computing the vorticity by taking the curl of Equation (2). The longitudinal component of the vorticity contains various terms that sustain the meridional balance (see, e.g., Miesch & Hindman 2011; Passos et al. 2017, for derivation and discussion). The inertial, \mathcal{I} , and the baroclinic, \mathcal{B} , terms are the most relevant (Kitchatinov et al. 2013), leading to the thermal wind balance (TWB) equation,

$$\mathcal{I} = \varpi \frac{\partial \Omega^2}{\partial z} = \mathcal{B} + \mathcal{D} = \frac{g}{\Theta_r} \frac{\partial \Theta'}{\partial \theta} + \mathcal{D}, \quad (21)$$

where z is the vertical axis in cylindrical coordinates, such that $\partial_z = \cos \theta \partial_r - r^{-1} \sin \theta \partial_\theta$, and \mathcal{D} incorporates all other forces

in the meridional plane, including the contribution of turbulent stresses, the turbulent baroclinicity, and the viscous forces (Miesch & Hindman 2011; Passos et al. 2017).

Departures from the TWB due to fluctuations of the LHS term induce meridional motions via the gyroscopic pumping seen from Equation (19). Similarly, latitudinal differential temperatures result in meridional flows driven by baroclinicity. Equations (19) and (21) are obviously coupled. As mentioned above, meridional motions are necessary to balance the angular momentum; these motions are generated by deviations from the TWB. Figure 15 shows the temperature fluctuations as a function of latitude. From the figure, it is possible to determine whether the gyroscopic pumping or the baroclinic force drives the meridional flow. For better visualization of the latitudinal differential temperature, two different scales are considered to the left and right of panels (a) to (c), corresponding to simulations R1x24 to R4x24, respectively. The scale on the left (right) Y-axis shows T' at the top (bottom) of the convective layer. Comparing the blue and red curves indicates that the latitudinal contrast is small (less than one degree) at the top of the domain, yet it reaches tens of Kelvins at the bottom of the CZ. Furthermore, at the top of the domain, the equator is colder than the poles for all cases, but below the CZ, the equator is colder only for simulation R1x24, and a large temperature contrast between a warmer equator and colder poles is found for simulation R4x24. The shadows show the deviation from the mean.

Given the profiles of Figure 15, baroclinicity should result in motions with prominent clockwise circulation for the case R1x24, and prominent counterclockwise circulation for cases R2x24 and R4x24. This is clearly not observed in the rightmost panels of Figure 12, except perhaps at intermediate to higher latitudes in case R4x24. The main source of the meridional motions observed outside the tangent cylinder is likely the departure from thermal wind balance about the inertia term, \mathcal{I} , which corresponds to the gyroscopic pumping.

The contribution of the meridional forces to the generation of meridional circulation can be better understood through the comparison of the two most important terms of the meridional force balance equation, namely the inertial, \mathcal{I} , and the baroclinic, \mathcal{B} , terms. If the two terms cancel each other, the system is in TWB. Whenever the balance is violated, either transiently or after temporal and longitudinal averages, vorticity in the meridional plane, i.e., meridional circulation, is induced. Figure 16 shows the contours of \mathcal{I} (first column) and \mathcal{B} (second column) in the meridional plane. The third column shows the departure of TWB via the residual $\mathcal{B} - \mathcal{I}$.

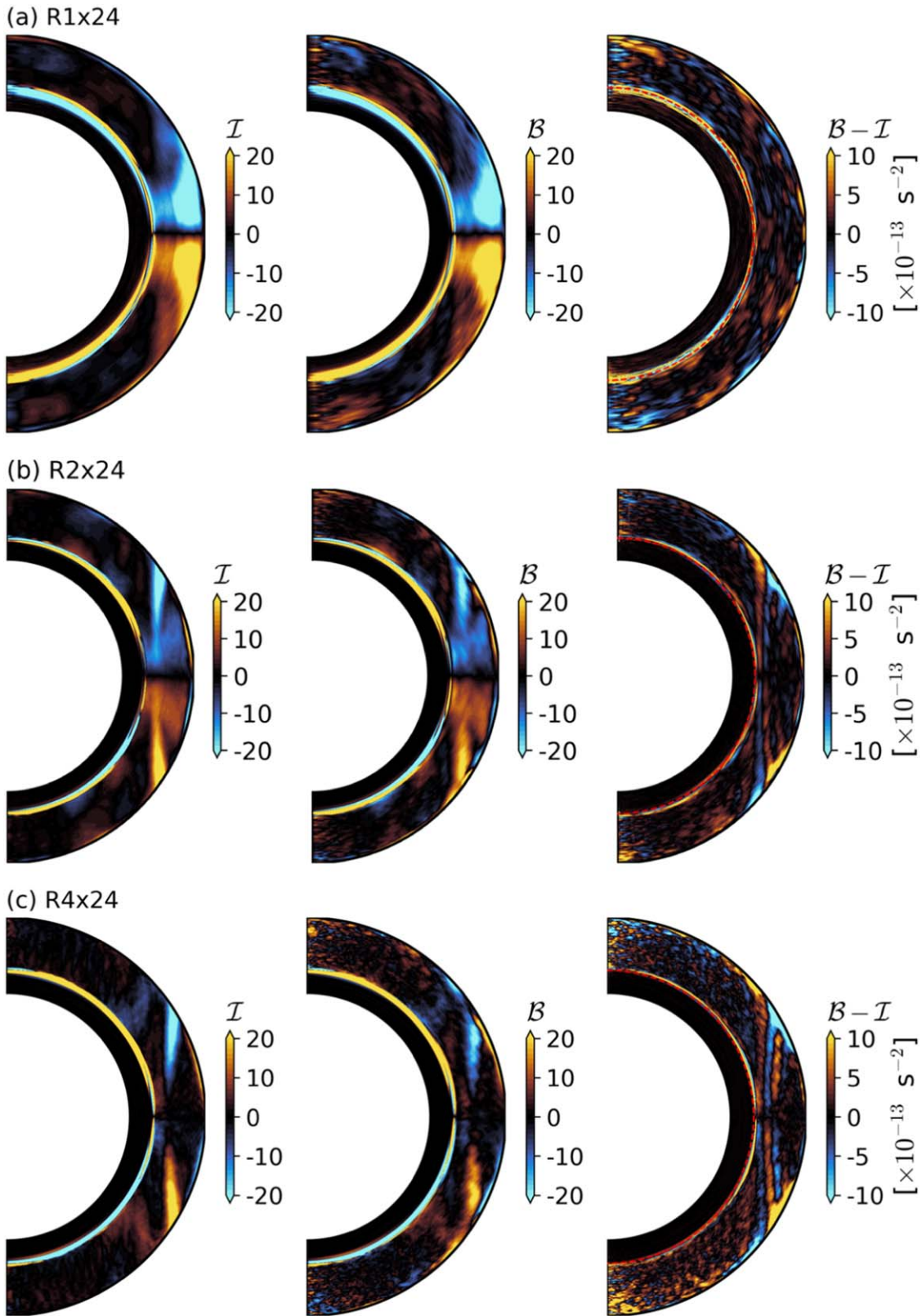


Figure 16. The inertia, \mathcal{I} (left), and baroclinic, \mathcal{B} (middle), terms of the TWB, Equation (21). The right column shows the residual $\mathcal{B} - \mathcal{I}$.

The first thing to notice in Figure 16 is the qualitative and quantitative similarities of the meridional profiles \mathcal{I} and \mathcal{B} . However, the third column shows that the balance is not perfect. Note that the scale of the residual is half of the inertial and baroclinic terms. Thus, the deviation from TWB is smaller

yet considerable. As expected, this deviation is more prominent outside the tangent cylinder, where the meridional circulation cells are observed. Not surprisingly, it increases with the numerical resolution providing enhanced meridional circulation (note that the opposite happens with the axial

torques, Figure 14, i.e., the residual decreases with the increase of resolution).

The departures from the TWB by meridional drivers, such as the meridional Reynolds stress component, sustain a meridional flow that is stronger at higher resolution because the numerical viscosity offers less and less resistance to these motions. The rightmost panels of Figures 17(a)—(c) in Appendix A show that the meridional component of the RS is indeed enhanced with the increase of resolution. The meridional motions compensate for the angular momentum transported by the Reynolds stresses. In the low-resolution case, where viscosity is high, the angular momentum balance due to MC is insufficient and the positive (negative) values of I_{θ}^{RS} in the northern (southern) hemisphere efficiently accelerate the equator. In the high-resolution case, the MC motions develop with less friction and better compensate for the angular momentum fluxes (see I_{θ}^{MC} in Figure 13). They are sufficiently strong to accelerate the poles. In the Sun, the molecular viscous resistance is insignificant. However, there is always the magnetic field, which may provide large- or small-scale Maxwell stresses, causing an effective equatorial transport of angular momentum and resulting in solar-like rotation. Yet it is not the only possibility to solve this issue.

In mean-field models of differential rotation (see Kitchatinov et al. 2013, for a review), the TWB is almost exact in the bulk of the convection zone. And departures are obtained at the boundary layers in such a way that a strong poleward meridional flow develops at the near-surface shear layer, and the equatorial return flow occurs at tachocline levels. The theory for the formation of the near-surface shear layer (NSSL) developed by Miesch & Hindman (2011) is in agreement with this view, suggesting that, in this layer, the inertia term is balanced by turbulent stresses rather than by the baroclinic force. It is worth remarking that, in the simulations presented here, the NSSL is not considered, and these boundary effects may be a relevant missing element. Nonetheless, baroclinicity is not sufficient to balance the inertial meridional force as presented above. It is possible that the turbulent motions developed in most of the current global simulations are not a reliable representation of the high Re, low Pr turbulence occurring inside the Sun.

Another remarkable point from Figure 16 is that the tachocline does not seem to act as a boundary layer generating strong departures of the TWB as suggested in mean-field models. It has usually been assumed that latitudinal gradients of temperature may be responsible for the deviation from the cylindrical toward the conical isorotation contours observed in the Sun. This seems to work in global simulations that do not include the tachocline where a latitudinal differential temperature is imposed as a boundary condition (Miesch et al. 2006). The simulations presented in this work, including the tachocline, demonstrate otherwise. Consider, for instance, the low-resolution simulation, R1x24. The slower north pole and fast equator make the variation of $\bar{\Omega}$ along the direction of the rotation axes (z) more negative at the poles than at $\sim 40^\circ$, where the convection zone rotates at the same speed as the stable layer. This is compensated by a negative gradient of Θ' , and consequently, in T' . Conversely, in case R4x24, $\bar{\Omega}$ goes from a slower stable layer toward a faster north pole, generating a positive signal for the term \mathcal{I} . This is compensated by a positive temperature gradient of ~ 40 K, which is also evident in \mathcal{B} . Therefore, it is possible to

conclude that, in our simulations, the differential temperature is a reaction of the baroclinic force to the gradient of the angular velocity in the z direction. Once the balance is established, the outcome is roughly cylindrical isorotation contours, independently of the rotation being faster at the equator or the poles.

4. Conclusions

We have performed HD convection simulations with the EULAG-MHD code in a spherical shell whose thermodynamic stratification resembles the upper part of the solar radiation layer and the convection zone up to $r = 0.96R_{\odot}$. We have considered cases without and with rotation. The thermal driving, considered here through an ambient state, results in an enthalpy flux corresponding to $\sim 0.3L_{\odot}$ for the nonrotating cases and $\sim 0.2L_{\odot}$ for the rotating simulations. Keeping fixed all the parameters in the governing equations, we explore how progressively increasing the numerical resolution affects the simulation results. We solve the equations in their inviscid form; therefore, the dissipation of momentum and heat is delegated only to truncation terms of the numerical method. Arguably, in this formulation we can achieve larger values of the effective Reynolds number with less computational resources than in a formulation with explicit dissipation terms. It is expected that, at sufficiently high Re, the contribution of viscosity to the transport of linear and angular momentum should be negligible and the dynamics of the system is defined by the properties of the turbulent motions. Our main goals are to identify the properties of the fluid as a function of the resolution and evaluate the challenges of achieving grid-independent results for this complicated problem.

For the nonrotating cases, our findings can be summarized as follows:

1. The low-order velocity moments and turbulent spectra of the nonrotating simulations do not show significant changes between the highest-resolution cases R4 and R8, indicating that the ILES convergence may be achieved at a resolution not much higher than R8. The estimates of the effective viscosity, ν_{eff} , and thermal conductivity, κ_{eff} , presented in Appendix B, show a sharp decrease with the increase of the longitudinal resolution, N_{ϕ} . For simulations R1–R8, their values are one to three orders of magnitude smaller than the turbulent viscosity, ν_t , respectively. Therefore, we believe that in the highest-resolution cases the dissipative processes are dominated by the resolved turbulent motions.
2. The ambient state considered in the model captures the sharp transition in the Brunt–Väisälä frequency at the bottom of the convection zone. High resolution in the radial direction is needed for this transition to be captured by the velocity field, especially its horizontal components. The gradient of U_{rms} between the stable and unstable layers increases with N_r but seems to saturate at $N_r = 256$ grid points (this value corresponds to a radial grid size $dz = 982$ km). This resolution also appears sufficient to capture the 4.5 density scale heights considered in the model (3.7 of which are in the convection zone).
3. The convective motions resulting from cases R4 and R8 are characterized by anisotropic convection, with most of the energy in the divergent component of the horizontal flow at the top of the domain. Because of the convection

zone thickness, the power spectra peak at larger scales, 1000–1400 Mm ($\ell \sim 3-4$), in good agreement with similar simulations performed with a much higher resolution (Hotta et al. 2014, 2019). There is also agreement with some characteristics of supergranulation obtained by Rincon et al. (2017). These motions, of course, have maximum energy at much smaller scales, presumably because they are driven by thermal perturbations injected into a thin boundary layer.

4. In case R1x, we increased the resolution of the simulation in the r direction and kept N_ϕ and N_θ equal to case R1. Despite the lack of detailed small-scale structures, the flow properties of this case correlate well with those obtained for cases R4 and R8. For this reason, we consider this resolution our starting point for the rotating simulations.

More important for the solar dynamics is the case of rotating convection. We performed three simulations where the radial grid size is kept constant, and only the horizontal resolution is increased. These cases appear in Table 1 as R1x24, R2x24, and R4x24. The rotation period of these simulations is 24 days. It is slightly shorter than the solar period, yet it results in solar-like differential rotation in the lower-resolution experiment, R1x24. The main results of these simulations are summarized below:

1. The perturbations of Θ , and more importantly, the luminosity carried by the enthalpy flux, are roughly the same for all simulations. Nevertheless, the amplitude of the velocity components increases with the resolution. This is more evident in the rms profile of the radial component, w_{rms} . The difference seems to be larger between R4x24 and R2x24 than between R2x24 and R1x24. This suggests that, for simulations accounting for the rotation, grid-independent solutions are hard to achieve.
2. The turbulent kinetic spectra shows strongly anisotropic motions near the top of the convection zone. The anisotropy decreases at the middle and bottom of the convection zone. As expected, rotation imprints vorticity in the flow. Thus, the energy of the toroidal part of the horizontal flows becomes dominant. Interestingly, the scale with maximal energy in the horizontal motions appears to be independent of the grid size. On the other hand, the energy in the radial component increases with the resolution, and the peak of the spectrum shifts toward larger harmonic degrees, i.e., the smaller scales become more energetic. This seems to be a robust result when comparing our findings with those of the high-resolution simulation of Miesch et al. (2008).
3. The change in the resulting mean flows as a function of grid resolution is dramatic. The output values of the Rossby number go from ~ 0.56 to ~ 0.65 , and in this range, we observe a transition from solar-like to antisolar differential rotation. The meridional circulation shows multiple cells aligned to the cylinder tangential to the tachocline. The meridional speed increases with the resolution, as well as with the high-latitude poleward flow.
4. The physics behind the differential rotation transition is understood through the integrated angular momentum balance and thermal wind balance (TWB). It may be summarized as follows. At low resolution, the total viscosity is high, one order of magnitude smaller than our

estimate of the turbulent viscosity, ν_t ; this offers strong resistance to the meridional motions driven by transient departures of the TWB. In this case, the angular momentum balance in the latitudinal direction is dominated by the viscosity and the Reynolds stresses, which pump angular momentum toward the equator. With the increase of the resolution, the effective viscosity decreases following a power law, becoming two orders of magnitude smaller than ν_t . Thus, there is a better angular momentum balance between the Reynolds stresses and the meridional circulation, arguably the most relevant processes to account for in HD simulations. This angular momentum equilibrium favors polar acceleration because there is a steady departure in the meridional force balance, and strong poleward meridional flows carry angular momentum with low friction.

5. In the simulations presented here, the latitudinal variations of temperature at the base of the convection zone are a consequence of TWB and not the result of departure from TWB as commonly assumed (see the concluding paragraph in Section 3.2.3). Thus, although there are strong temperature gradients between the equator and pole, the contours of isorotation are roughly cylindrical.

The results presented here correspond to an enthalpy flux carrying only one-fourth of the solar luminosity, and the rotation period is compatible with the sidereal rotation period of the Sun. Extrapolating the observed trend to solar values would result in a larger discrepancy with the solar differential rotation. Also, the energy contained in scales corresponding to $\ell \sim 30-40$ would be higher than what is found in recent solar observations (Proxauf 2020), suggesting that increasing the resolution does not lead to a solution of the convective conundrum. These problems, of course, are not specific to the EULAG-MHD simulations but are present in most global convection models. The results of the recent simulations of Hotta & Kusano (2021) and Hotta et al. (2022) suggest that the small-scale dynamo might be a solution. This field may act as friction that quenches the velocity and contributes to the angular momentum balance, leading to solar-like rotation. Other MHD simulations indicate that the large-scale magnetic field may contribute in the same direction (Fan & Fang 2014; Guerrero et al. 2016; Karak et al. 2015). To this date, there are no simulations where both small- and large-scale contributions of the magnetic field, the usual suspect, are considered.

Nonetheless, the entire problem may reside in the fact that the convection driven in the global simulations is not an accurate representation of the turbulent motions in the solar interior. The reason for this could be the enormous differences in the parameter regime between the Sun and the simulations. It has also been suggested that the deep solar convection may depend on the physics occurring in the uppermost 50 Mm (or less) of the Sun (Spruit 1997), which are barely considered in global simulations. In this boundary layer, the effective cooling provided by hydrogen ionization destabilizes the plasma, generating cold downward plumes. Thus, the turbulent motions in the deep solar convection zone may be driven by this penetrative entropy rain (Brandenburg 2016). In this sense, deep solar convection can be seen as a nonlocal process in a buoyantly neutral layer. The numerical experiments performed by Cossette & Rast (2016) demonstrated this concept in a Cartesian box. Their results show that the dominant convective scales depend on the thickness of the boundary layer.

Concurrently, the fast convective motions in this layer are not constrained by the solar rotation, and they produce a negative shear that, in turn, accelerates meridional motions, producing the observed surface latitudinal velocity (Miesch & Hindman 2011). Recent simulations by Kitiashvili et al. (2022) showed that turbulent convection in the upper part of the NSSL can generate radial differential rotation and meridional circulation. However, it is still uncertain how the turbulent correlations generated by nonlocal convection can sustain the solar differential rotation below the NSSL. Thus, it is worth exploring this possibility and its consequences for the mean flows in global simulations. The pursuit of numerical convergence is also worth more computational efforts. A database of simulations with varying resolutions is necessary for studying the changes in the turbulence properties at different Rayleigh and Reynolds numbers. It can also be used for the experimentation of subgrid-scale methods that allow realistic simulations at a lower computational cost. These goals will be pursued in future works.

We thank the anonymous referee for the constructive comments and suggestions that have improved the quality of the paper. We thank Bonnie Zaire for her comments on the manuscript. This work was partly funded by NASA grants NNX14AB70G, 80NSSC20K0602, and 80NSSC20K1320. NCAR is sponsored by the National Science Foundation. A. Strugarek acknowledges support from the French Programme National Soleil Terre (INSU) and from Solar Orbiter CNES funds. The simulations were performed in the NASA super-computer Pleiades

Appendix A Reynolds Stresses

For completeness, Figure 17 of this appendix presents the Reynolds stresses obtained from the rotating simulations (a) R1x24, (b) R2x24, and (c) R4x24. The stresses are defined as

$$\mathcal{R}_{\phi\theta} = \overline{u'v'}, \quad \mathcal{R}_{\phi r} = \overline{u'w'}, \quad \mathcal{R}_{\theta r} = \overline{v'w'}. \quad (\text{A1})$$

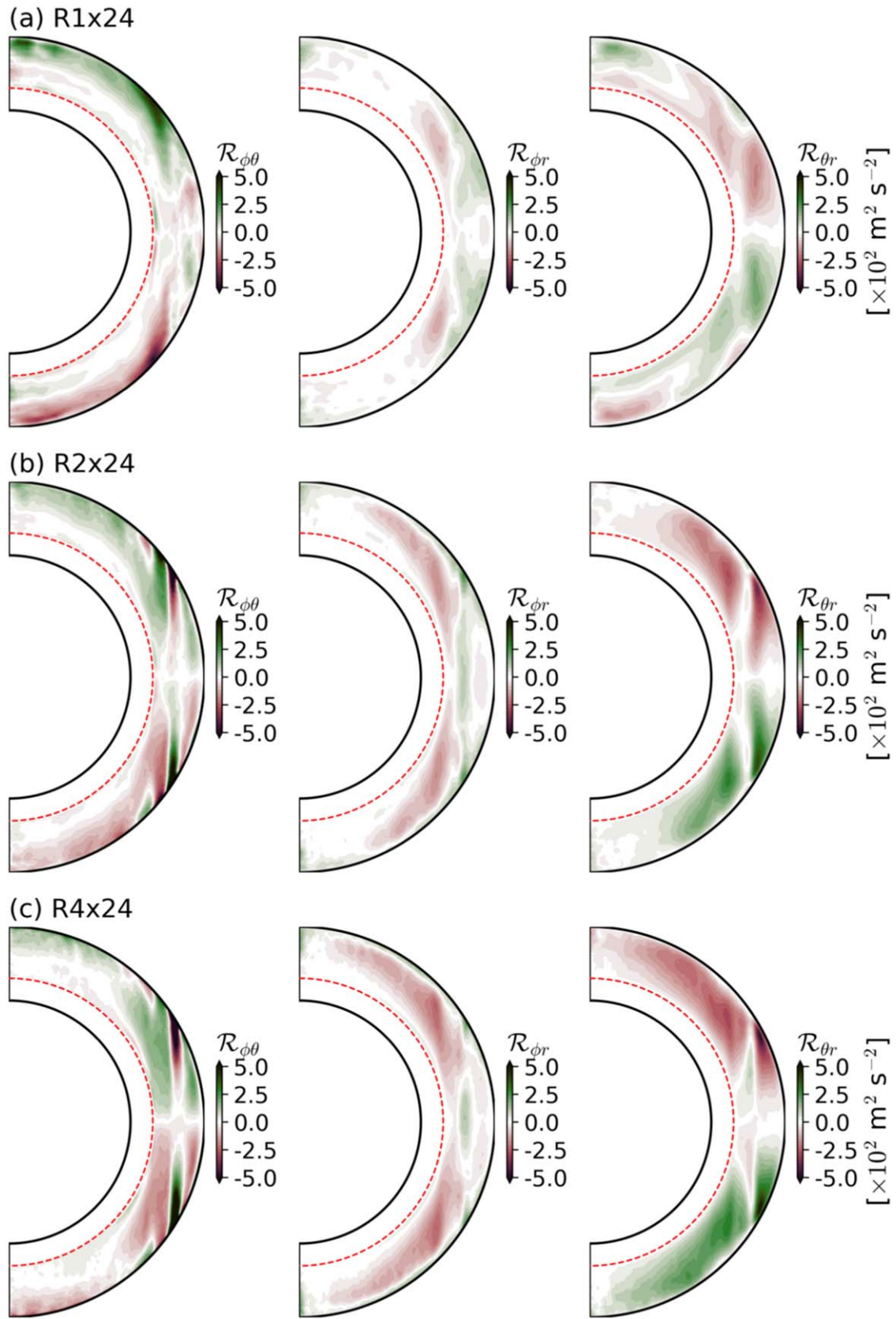


Figure 17. Reynolds stresses resulting from simulations (a) R1x24, (b) R2x24, and (c) R4x24.

Appendix B

Estimation of Effective Viscosity and Thermal Diffusion

Estimated values of the effective viscosity and the thermal conduction are computed by using the procedure presented in Strugarek et al. (2016). It consists of evaluating kinetic and thermal energy transfer functions in the spherical harmonics space. There is one function for each term of Equations (2) and (3). In a steady state, the sums of these terms are equaled to the viscous stress vector and the Fickian thermal diffusion for the velocity and the perturbations of potential temperature, respectively. The method allows estimating effective viscosity, ν_{eff} , and thermal conduction, κ_{eff} , as a function of wavenumber and radius. In the spectral space, dissipative terms are proportional to the square of the wavenumber; therefore, only the largest wavenumbers for each resolution are considered, i.e., the results represent the coefficients dissipating the smallest resolved scales. The radial profiles of ν_{eff} and κ_{eff} are presented in Figures 18(a) and (b), respectively. The colors correspond to the nonrotating simulations R1 (solid black), R2 (blue), R4 (red), R8 (green), and R1x (dashed black line). The

shadows show the standard deviation along the considered wavenumbers. As motions and thermal fluctuations are small in the stably stratified layer, the resulting coefficients have large errors. For this reason, the figure presents only the profiles in the convection zone. Averaging the profiles of Figure 18(a) and (b) over radius allows the construction of scaling laws for ν_{eff} and κ_{eff} as a function of the resolution in the longitudinal direction, N_ϕ . The results are presented in panel (c).

The results for the rotating cases are presented in Figures 19(a) and (b). The colors correspond to simulations R1x24 (blue), R2x24 (red), and R4x24 (green). The scaling laws are presented in panel (c). Note that, in these cases, the grid size in the radial direction remains constant and only changes in the latitudinal and longitudinal direction. This explains the flatter scaling laws. It is worth remarking that several approximations were made to compute the dissipation coefficients. Therefore, these values are physical estimates and do not correspond to the exact numerical dissipation of the MPDATA scheme, which is nonlinear and intermittent in space and time.

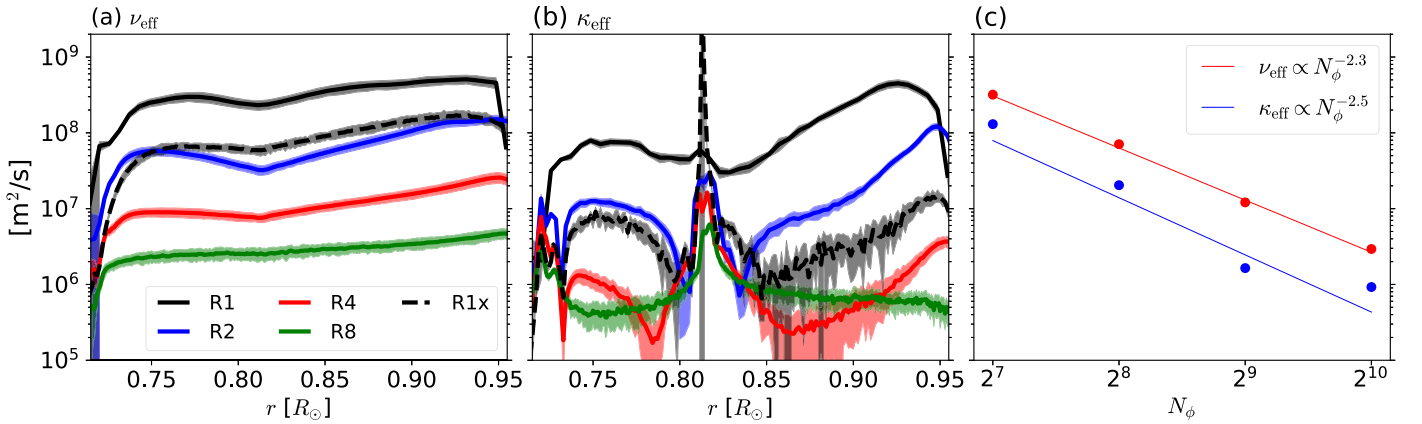


Figure 18. Radial profiles of the effective viscosity, ν_{eff} (panel a), and the thermal conductivity κ_{eff} for the nonrotating simulations represented with different colors. The shadows show the standard deviation for the highest wavenumbers resolved in each simulation. The average value over the convection zone as a function of the longitudinal resolution N_ϕ is presented in panel (c). The thin continuous line shows the corresponding scaling laws.

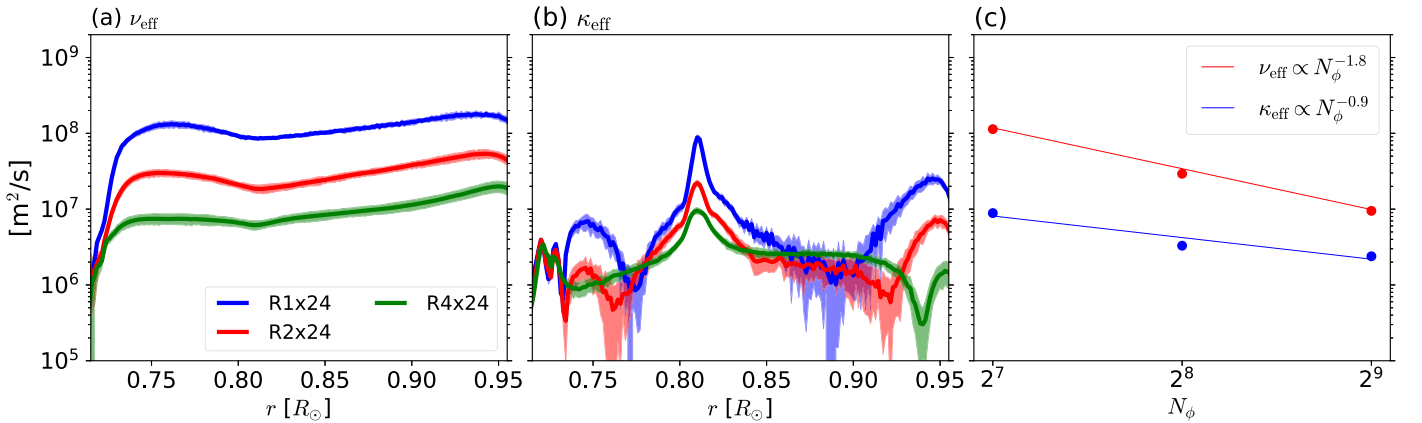


Figure 19. Same as Figure 18 but for the rotating simulations R1x24 (blue line in panels (a) and (b)), R2x24 (red), and R4x24 (green).

ORCID iDs

G. Guerrero  <https://orcid.org/0000-0002-2671-8796>
 A. M. Stejko  <https://orcid.org/0000-0001-7483-3257>
 A. G. Kosovichev  <https://orcid.org/0000-0003-0364-4883>
 P. K. Smolarkiewicz  <https://orcid.org/0000-0001-7077-3285>
 A. Strugarek  <https://orcid.org/0000-0002-9630-6463>

References

- Böhm-Vitense, E. 1958, *ZAp*, **46**, 108
 Brandenburg, A. 2016, *ApJ*, **832**, 6
 Brown, B. P., Browning, M. K., Brun, A. S., Miesch, M. S., & Toomre, J. 2008, *ApJ*, **689**, 1354
 Brun, A. S., & Toomre, J. 2002, *ApJ*, **570**, 865
 Busse, F. H., & Or, A. C. 1986, *JFM*, **166**, 173
 Chen, R., & Zhao, J. 2017, *ApJ*, **849**, 144
 Christensen-Dalsgaard, J., Dappen, W., Ajukov, S. V., et al. 1996, *Sci*, **272**, 1286
 Cossette, J.-F., Charbonneau, P., Smolarkiewicz, P. K., & Rast, M. P. 2017, *ApJ*, **841**, 65
 Cossette, J.-F., & Rast, M. P. 2016, *ApJL*, **829**, L17
 Fan, Y., Abbett, W. P., & Fisher, G. H. 2003, *ApJ*, **582**, 1206
 Fan, Y., & Fang, F. 2014, *ApJ*, **789**, 35
 Featherstone, N. A., & Hindman, B. W. 2016a, *ApJ*, **818**, 32
 Featherstone, N. A., & Hindman, B. W. 2016b, *ApJL*, **830**, L15
 Featherstone, N. A., & Miesch, M. S. 2015, *ApJ*, **804**, 67
 Gastine, T., Yadav, R. K., Morin, J., Reiners, A., & Wicht, J. 2014, *MNRAS*, **438**, L76
 Getling, A. V., & Kosovichev, A. G. 2022, *ApJ*, **937**, 1
 Ghizaru, M., Charbonneau, P., & Smolarkiewicz, P. K. 2010, *ApJL*, **715**, L133
 Gizon, L., & Birch, A. C. 2012, *PNAS*, **109**, 11896
 Gizon, L., Cameron, R. H., Pourabdian, M., et al. 2020, *Sci*, **368**, 1469
 Greer, B. J., Hindman, B. W., Featherstone, N. A., & Toomre, J. 2015, *ApJL*, **803**, L17
 Grinstein, F., Margolin, L., & Rider, W. 2007, *Implicit Large Eddy Simulation: Computing Turbulent Fluid Dynamics* (Cambridge: Cambridge Univ. Press)
 Guerrero, G., Smolarkiewicz, P. K., de Gouveia Dal Pino, E. M., Kosovichev, A. G., & Mansour, N. N. 2016, *ApJL*, **828**, L3
 Guerrero, G., Smolarkiewicz, P. K., Kosovichev, A. G., & Mansour, N. N. 2013, *ApJ*, **779**, 176
 Guerrero, G., Zaire, B., Smolarkiewicz, P., et al. 2019, *ApJ*, **880**, 6
 Hanasoge, S. M., Duvall, T. L., & Sreenivasan, K. R. 2012, *PNAS*, **109**, 11928
 Hathaway, D. H., & Upton, L. 2014, *JGRA*, **119**, 3316
 Hathaway, D. H., & Upton, L. A. 2021, *ApJ*, **908**, 160
 Hindman, B. W., Featherstone, N. A., & Julien, K. 2020, *ApJ*, **898**, 120
 Hotta, H. 2018, *ApJL*, **860**, L24
 Hotta, H., Iijima, H., & Kusano, K. 2019, *SciA*, **5**, 2307
 Hotta, H., & Kusano, K. 2021, *NatAs*, **5**, 1100
 Hotta, H., Kusano, K., & Shimada, R. 2022, *ApJ*, **933**, 199
 Hotta, H., Rempel, M., & Yokoyama, T. 2014, *ApJ*, **786**, 24
 Hotta, H., Rempel, M., & Yokoyama, T. 2015, *ApJ*, **798**, 51
 Käpylä, P. J., Käpylä, M. J., & Brandenburg, A. 2014, *A&A*, **570**, A43
 Käpylä, P. J., Mantere, M. J., Guerrero, G., Brandenburg, A., & Chatterjee, P. 2011, *A&A*, **531**, A162
 Karak, B. B., Käpylä, P. J., Käpylä, M. J., et al. 2015, *A&A*, **576**, A26
 Kippenhahn, R., Weigert, A., & Weiss, A. 2013, *Stellar Structure and Evolution* (Berlin: Springer)
 Kitchatinov, L. L. 2013, in *Proc. IAU 294, Solar and Astrophysical Dynamos and Magnetic Activity*, ed. A. G. Kosovichev, E. de Gouveia Dal Pino, & Y. Yan (Cambridge: Cambridge Univ. Press), 399
 Kitiashvili, I. N., Kosovichev, A. G., Mansour, N. N., & Wray, A. A. 2015, *ApJ*, **809**, 84
 Kitiashvili, I. N., Kosovichev, A. G., Wray, A. A., Sadykov, V. M., & Guerrero, G. 2022, arXiv:2203.01484
 Kolmogorov, A. 1941, *DoSSR*, **30**, 301
 Lipps, F. B., & Hemler, R. S. 1982, *JatS*, **39**, 2192
 Miesch, M. S., Brun, A. S., DeRosa, M. L., & Toomre, J. 2008, *ApJ*, **673**, 557
 Miesch, M. S., Brun, A. S., & Toomre, J. 2006, *ApJ*, **641**, 618
 Miesch, M. S., & Hindman, B. W. 2011, *ApJ*, **743**, 79
 Nogueira, H. D., Guerrero, G., Smolarkiewicz, P. K., & Kosovichev, A. G. 2022, *ApJ*, **928**, 148
 Ossendrijver, M. 2003, *A&ARv*, **11**, 287
 Passos, D., Miesch, M., Guerrero, G., & Charbonneau, P. 2017, *A&A*, **607**, A120
 Proxauf, B. 2020, PhD thesis, Georg August Univ. of Göttingen, Germany
 Prusa, J. M., Smolarkiewicz, P. K., & Wyszogrodzki, A. A. 2008, *CF*, **37**, 1193
 Rincon, F., & Rieutord, M. 2018, *LRSP*, **15**, 6
 Rincon, F., Roudier, T., Schekochihin, A. A., & Rieutord, M. 2017, *A&A*, **599**, A69
 Rogachevskii, I., Kleorin, N., Kitiashvili, I. N., et al. 2011, arXiv:1102.1206
 Schaeffer, N. 2013, *GGG*, **14**, 751
 Scherrer, P. H., Schou, J., Bush, R. I., et al. 2012, *Sol. Phys.*, **275**, 207
 Schou, J., Antia, H. M., Basu, S., et al. 1998, *ApJ*, **505**, 390
 Smolarkiewicz, P. K. 2006, *IJNMF*, **50**, 1123
 Smolarkiewicz, P. K., & Charbonneau, P. 2013, *JCoPh*, **236**, 608
 Spiegel, E. A., & Zahn, J. P. 1992, *A&A*, **265**, 106
 Spruit, H. C. 1997, *Mem. Soc. Astron. Italiana*, **68**, 397
 Stejko, A. M., Kosovichev, A. G., & Pipin, V. V. 2021, *ApJ*, **911**, 90
 Strugarek, A., Beaudoin, P., Brun, A. S., et al. 2016, *AdSpR*, **58**, 1538
 Strugarek, A., Beaudoin, P., Charbonneau, P., Brun, A. S., & do Nascimento, J.-D. 2017, *Sci*, **357**, 185
 Ulrich, R. K. 2010, *ApJ*, **725**, 658
 Wray, A. A., Bensassi, K., Kitiashvili, I. N., Mansour, N. N., & Kosovichev, A. G. 2015, arXiv:1507.07999